

# GAMA/DEVILS: constraining the cosmic star formation history from improved measurements of the 0.3–2.2 $\mu$ m extragalactic background light

Soheil Koushan,<sup>1</sup>★ Simon P. Driver,<sup>1</sup>★ Sabine Bellstedt<sup>1</sup>, Luke J. Davies<sup>1</sup>,★ Aaron S. G. Robotham<sup>1</sup>, Claudia del P. Lagos<sup>1,2</sup>, Abdolhosein Hashemizadeh<sup>1</sup>, Danail Obreschkow<sup>1</sup>, Jessica E. Thorne<sup>1</sup>, Malcolm Bremer<sup>3</sup>, B. W. Holwerda<sup>4</sup>, Andrew M. Hopkins<sup>5</sup>, Matt J. Jarvis<sup>6</sup>, Malgorzata Siudek<sup>7,8</sup> and Rogier A. Windhorst<sup>9</sup>

<sup>1</sup>ICRAR, The University of Western Australia, 35 Stirling Highway, Crawley, WA 6009, Australia

<sup>2</sup>ARC Centre of Excellence for All Sky Astrophysics in 3 Dimensions (ASTRO 3D)

<sup>3</sup>Astrophysics Group, School of Physics, University of Bristol, Tyndall Avenue, Bristol BS8 1TL, UK

<sup>4</sup>Department of Physics and Astronomy, University of Louisville, 102 Natural Science Building, Louisville, KY 40292, USA

<sup>5</sup>Australian Astronomical Optics, Macquarie University, 105 Delhi Rd, North Ryde, NSW 2113, Australia

<sup>6</sup>Oxford Astrophysics, Denys Wilkinson Building, Keble Road, Oxford OX1 3RH, UK

<sup>7</sup>Institut de Física d'Altes Energies (IFAE), The Barcelona Institute of Science and Technology, E-08193 Bellaterra (Barcelona), Spain

<sup>8</sup>National Centre for Nuclear Research, ul. Hoza 69, PL-00-681 Warsaw, Poland

<sup>9</sup>School of Earth & Space Exploration, Arizona State University, Tempe, AZ 85287-1404, USA

Accepted 2021 February 19. Received 2021 February 19; in original form 2020 June 23

## ABSTRACT

We present a revised measurement of the optical extragalactic background light (EBL), based on the contribution of resolved galaxies to the integrated galaxy light (IGL). The cosmic optical background radiation (COB), encodes the light generated by star formation, and provides a wealth of information about the cosmic star formation history (CSFH). We combine wide and deep galaxy number counts from the Galaxy And Mass Assembly survey (GAMA) and Deep Extragalactic Visible Legacy Survey (DEVILS), along with the *Hubble Space Telescope* (HST) archive and other deep survey data sets, in nine multiwavelength filters to measure the COB in the range from 0.35  $\mu$ m to 2.2  $\mu$ m. We derive the luminosity density in each band independently and show good agreement with recent and complementary estimates of the optical-EBL from very high-energy (VHE) experiments. Our error analysis suggests that the IGL and  $\gamma$ -ray measurements are now fully consistent to within  $\sim 10$  per cent, suggesting little need for any additional source of diffuse light beyond the known galaxy population. We use our revised IGL measurements to constrain the CSFH, and place amplitude constraints on a number of recent estimates. As a consistency check, we can now demonstrate convincingly, that the CSFH, stellar mass growth, and the optical-EBL provide a fully consistent picture of galaxy evolution. We conclude that the peak of star formation rate lies in the range 0.066–0.076  $M_{\odot} \text{ yr}^{-1} \text{ Mpc}^{-3}$  at a lookback time of 9.1 to 10.9 Gyr.

**Key words:** methods: data analysis – galaxies: evolution – galaxies: statistics – cosmology: cosmic background radiation – cosmological parameters – diffuse radiation.

## 1 INTRODUCTION

The extragalactic background light (EBL) is defined as the total flux received today ( $\text{nW m}^{-2} \text{ steradian}^{-1}$ ) from all sources of photon production since the epoch of recombination plus the cosmic microwave background (CMB). The CMB component is somewhat distinct, as it represents the radiation field from the epoch of recombination as the temperature, pressure, and density of the Universe dropped to the point where nuclei and electrons combined to form neutral atoms (Hauser & Dwek 2001; Kashlinsky 2006; Cooray et al. 2009;

Grazian et al. 2009; Domínguez et al. 2011; Inoue et al. 2013; Driver et al. 2016b). Hence, the EBL represents the integrated luminosity cone of the Universe from the CMB surface to the present day. Understanding this energy is essential as it encodes all photon production pathways. This photon-energy production pervades the entire electromagnetic spectrum, but is typically broken into distinct wavelength ‘windows’ (see Hill, Masui & Scott 2018), aligned with the detection technologies.

Overall, the CMB, the redshifted thermal remnant of the hot early Universe (Penzias & Wilson 1965), is the dominant component of the EBL. The subsequent photon production represents the remainder of the EBL, and has been produced by stars, gas, accreting black holes (BHs) and dust emission – and other processes – arising over the entire path-length of the Universe (i.e. since  $\sim 380\,000$  yr after the

\* E-mail: [so.koushan@gmail.com](mailto:so.koushan@gmail.com) (SK); [simon.driver@uwa.edu.au](mailto:simon.driver@uwa.edu.au) (SPD); [luke.j.davies@uwa.edu.au](mailto:luke.j.davies@uwa.edu.au) (LJD)

big bang). The CMB also dominates the energy distribution of the EBL, being a factor of  $\sim 40$  times higher ( $\sim 960 \text{ nW m}^{-2} \text{ sr}^{-1}$ ) than either the infrared or optical backgrounds (Scott 2000; Wright 2004; Dole et al. 2006; Driver et al. 2016b; Driver 2020).

The cosmic optical background (COB) light is the second most important part of the EBL in terms of photon production, and is tied with the cosmic infrared background (CIB) in terms of final photon density and integrated photon energy (NB: most CIB photon energy originates from photons produced in the COB, which are absorbed and re-radiated to form the CIB, hence the COB dominates in terms of photon production). The COB is one of the least well-known components of the EBL spectra, primarily due to the uncertainties in subtracting the intervening foregrounds. Formally, the COB is defined to be the emission emitted in the wavelength range from  $0.1 \mu\text{m}$  to  $8 \mu\text{m}$  (i.e. the UV to mid-infrared, MIR), and arises primarily from the formation and evolution of stellar mass as galaxies form and evolve (Hauser & Dwek 2001). Hence, the energy density of the COB is closely related to the growth of stellar mass over all time (Bernstein 1999). There is also a non-negligible contribution from active galactic nuclei (AGNs) whereby light, due to the accretion on to a supermassive BH, escapes from the host galaxy and radiates through the inter-galactic medium (e.g. Matsuoka et al. 2011; Driver et al. 2016a).

The COB also encodes information about the entire cosmic star formation history (CSFH), as well as the origin and fate of the very first stars responsible for reionization that constitutes 0.1 to 1 per cent of the total EBL (Cooray et al. 2009; Windhorst et al. 2018). The reasons above make the COB one of the most highly studied portions of the background light with tremendous potential to provide strong astrophysical constraints on galaxy formation and evolution.

At longer wavelengths, the CIB light is defined as emission at wavelengths between  $8 \mu\text{m}$  and  $1000 \mu\text{m}$  (Puget et al. 1996; Lagache et al. 1999; Hauser & Dwek 2001; Kashlinsky 2006). As mentioned, a significant amount of the starlight produced at UV and optical wavelengths, is absorbed by dust in the host galaxies and later re-radiated in MIR to far-infrared (FIR), contributing to the CIB. The CIB spectral energy distribution (SED) has a peak of the emission at  $100 \mu\text{m}$  equating to thermal dust emission with temperatures in the range 20–60 K. As detected from the Earth, both the COB and CIB have approximately the same contribution of  $24$  and  $26 \text{ nW m}^{-2} \text{ sr}^{-1}$ , respectively (Driver et al. 2016b). Thus, the combination of the IR and optical background light equates, energy-wise, to about  $\sim 5$  per cent of the CMB.

Unfortunately, despite significant efforts, the current measurements of the COB and CIB exhibit significant inconsistencies most likely associated with the measurement methods (see reviews by Hill et al. 2018; Mattila & Väisänen 2019; Driver 2020). Conventionally, these efforts are classified as direct (background sky brightness; Matsumoto et al. 2005; Matsuoka et al. 2011; Cooray et al. 2012; Zemcov et al. 2013, 2017; Kawara et al. 2017), and indirect (based on counting galaxies; Madau & Pozzetti 2000; Totani et al. 2001; Xu et al. 2005; Grazian et al. 2009; Keenan et al. 2010; Driver et al. 2016b).

Direct measurement is the traditional technique applied to estimate the COB, including both discrete and diffuse emission. This is based on detecting the absolute flux of the night sky from space platforms and subtracting the contributing foregrounds. The dominant foreground component outside of the Earth's atmosphere is the zodiacal dust glow. This foreground is caused by minuscule dust fragments reflecting sunlight and forming the so-called zodiacal light (ZL; Leinert et al. 1981; Bernstein, Freedman & Madore 2002; Aharonian et al. 2006). In addition to the ZL, the diffuse sky emission may

contain residual airglow (unless the observing platform is entirely beyond Earth's orbit), and diffuse galactic light (DGL). The optimal technique for separating the DGL and ZL + Airglow remains controversial (Kim et al. 2019). The intensity of the DGL is 5 to 10 times larger than the EBL, and the ZL + Airglow varies from 30 to 100 times the EBL (Mattila et al. 2012). These foregrounds are also time/day variable (i.e. ZL + Airglow), and so they need to be estimated for each observation. Therefore, searching for an optimized and well-established model to remove the foregrounds efficiently is of high priority. One suggested technique designed to overcome these backgrounds is the Dark Cloud method (Mattila et al. 2017a), in which the effect of the foregrounds on the background light is measured by estimating the differential measurement between a dark nebula at high galactic latitude and a surrounding clear region. This results in an upper limit to the UV and blue portion of the EBL.

The indirect method, alternatively, represents the integrated galaxy counts from deep observations and defines the entire photon flux from discrete sources (i.e. galaxies, quasars) only. In this work, we aim to measure the integrated galaxy light (IGL) from a compendium of wide and deep galaxy number count data from the optical to the near-infrared (NIR). By having sufficiently wide and deep photometric data, the EBL obtained from the galaxy count method should converge to that from direct measurements. The difference in the two methods can, in due course, provide constraints on any diffuse sources (see the discussion in Driver et al. 2016b). Over the past decades, there has been a rapid increase of new data provided by e.g. *Hubble Space Telescope* (HST COSMOS; Scoville et al. 2007, HST GOODS; Giavalisco et al. 2004, HST CANDLES; Grogin et al. 2011), *Spitzer* (Sanders et al. 2007, Frayer et al. 2009), *IRIS* (De Pontieu et al. 2014), *Gaia* (Gaia Collaboration 2016), *WISE* (Wright et al. 2010), and *Herschel* (Pilbratt et al. 2010). Along with the unprecedented number of new data from space-based facilities, there has been a major improvement in deep and wide surveys with ground-based telescopes. In particular: *ESO-VLT* (Vernet et al. 2009), *Pan STARRS* (Kaiser et al. 2002), *Subaru* (Taniguchi et al. 2007), and *CFHT* (Capak et al. 2007). Nevertheless, the discrepancy between direct and indirect methods is far larger than expected, and the subject of much debate (Mattila & Väisänen 2019). At present the discrepancy in the CIB estimates are  $\sim 75$  per cent, while in the COB the estimates vary by a factor of 3 to 5.

Recently, with the advancement of VHE facilities, another method has become successful at constraining the EBL by probing the  $\gamma$ -rays of distant blazars (e.g. MAGIC Collaboration 2008; Domínguez et al. 2011; VERITAS Collaboration 2011; Biteau 2013; Fermi-LAT Collaboration 2018, FL18; HESS Collaboration 2018). This technique relies on the interaction of high-energy TeV photons from blazars with the COB through  $\gamma$ - $\gamma$  absorption (Desai et al. 2017). Accordingly, this TeV to micron photon coupling allows the use of  $\gamma$ -rays to probe the optical portion of the EBL over the redshift range covered by the blazar distribution. The advantage of this approach, in comparison with direct estimation, is that it is unaffected by the foregrounds (ZL and Galactic emission), although arguably susceptible to intergalactic magnetic fields. At the present time, the IGL measurements (EBL estimates in the absence of any diffuse light) agree with the very high-energy (VHE), Dark Cloud, and are mostly consistent with the recent direct estimates from deep space probes (*New Horizon* and *Pioneer*, which observe from beyond the ZL and airglow). This consensus motivates us to improve our IGL analysis further by looking to reduce the inherent uncertainty from our previous IGL measurements of  $\sim 20$  per cent as reported by Driver et al. (2016b).

In Driver et al. (2016b), published data from a variety of sources was assembled spanning from far-UV (FUV) to FIR wavelengths, i.e. covering both the COB and CIB. These data were used to provide compilations of galaxy number-counts from bright to faint magnitudes and integrated to obtain FUV to FIR IGL estimates. The error analysis of that work indicated an uncertainty in the measurements of around 20 per cent stemming from several sources. In this paper, we look to make two improvements. The first is to replace the bright and intermediate data with a more homogeneous analysis where particular care has been taken to overcome fragmentation and false source detection. The second is an improved error-analysis, in particular an improvement in the sample variance handling and alignment of photometry on to a common filter set.

Through these improvements we look to improve the optical/NIR IGL uncertainty from 20 per cent to below 10 per cent, as well as identify the key areas for future improvement to eventually bring the uncertainties down to a few per cent. This paper is structured as follows: In Section 2, we summarize the newly processed data from various wide and deep surveys followed by the colour transformations to a common filter system. Section 3 shows the revised galaxy number-counts and the fitting process. In Section 4, we present our analysis for estimating the integrated galactic light of the optical EBL with an improved focus on error analysis. Comparison to VHE analysis and implications for missing diffuse light are discussed in Section 5. Finally, we constrain the CSFH using the EBL estimates described in Section 6.

Throughout this paper, all magnitudes are in the AB system and we assume a cosmology with  $H_0 = 70 \text{ km s}^{-1} \text{ Mpc}^{-1}$ ,  $\Omega_\Lambda = 0.7$ , and  $\Omega_M = 0.3$ .

## 2 NUMBER COUNT DATA

In Driver et al. (2016b), data for the optical/NIR IGL estimates were taken primarily from the Galaxy And Mass Assembly (GAMA), COSMOS, and *HST* surveys (*HST*/ACS/WFC3 + LBT/LBC + ESO VLT Hawk-I). Recently, improvements have been made in the analysis of both the GAMA and COSMOS photometry, using the new PROFOUND source finding code (Robotham et al. 2018; Bellstedt et al. 2020a; Davies et al., in preparation). Here, we exclusively focus on three contributing data sets: GAMA, DEVILS-COSMOS, and *HST*, as briefly described below.

### 2.1 GAMA

GAMA (Driver et al. 2011; Liske et al. 2015) is a spectroscopic (98 per cent completeness) multiwavelength campaign across  $\sim 230 \text{ deg}^2$  in the Northern and Southern Galactic caps, centred on R.A. = 2h, 9h, 12h, 14.5h, and 23h, with the AAOmega fiber spectrograph on the 3.9-m Anglo Australian Telescope (AAT; Hopkins et al. 2013). GAMA includes a panchromatic survey in 20 filters extending from the UV to the FIR (Driver et al. 2016a), composed of observations from various wide and deep ground-based (VST KiDS; VISTA VIKING) and space-based (*GALEX*; *WISE*; *Herschel*) facilities as summarized in Driver et al. (2016a). GAMA's main science goal is to quantify the evolution of mass, energy, and structure over the history of the cosmos (Driver & GAMA Team 2016; D18; Moffett et al. 2016). GAMA targets more than 200 000 galaxies to a depth of  $r < 19.8$  magnitude, and presents a panchromatic data set of galaxies from the low-redshift Universe ( $z < 0.3$ ).

Here, we use our reanalysis (Bellstedt et al. 2020a) of KiDS-DR4 optical-IR (Kuijken et al. 2019) and VISTA VIKING (Edge

et al. 2013) imaging of the GAMA regions with an effective area of  $\sim 217.5 \text{ deg}^2$ . Previously, GAMA optical photometry as used in Driver et al. (2016b), was based on SEXTRACTOR analysis of the SDSS data (see Driver et al. 2016b), whereas the reanalysis is based on PROFOUND (Robotham et al. 2018). Improvements include the use of dilated segments, watershed deblending, higher-resolution data (KiDS – SDSS), improved star–galaxy separation, extensive visual inspection, and manual fixing of fragmented galaxies (see Bellstedt et al. 2020a for full details). These enhancements improve the integrity of the counts at both very bright and intermediate magnitudes, as well as extending the data to fainter limits than was possible with the SDSS data, and in particular to the depths that dominate the IGL measurement.

### 2.2 DEVILS-COSMOS

The Deep Extragalactic Visible Legacy Survey (DEVILS; Davies et al. 2018), is a spectroscopic survey on the Anglo-Australian Telescope (AAT), sampling more than  $\sim 60\,000$  galaxies to a depth of  $Y < 21.2$  mag. DEVILS covers  $6 \text{ deg}^2$  of the sky aiming for more than 95 per cent completeness in three deep fields (COSMOS; Scoville et al. 2007, ECDFS; Virani et al. 2006, XMM-LSS; Pierre et al. 2004). Here, we adopted the up-to-date photometric catalogue for the D10 (COSMOS) and D02 (CMM-LSS) regions that cover  $\sim 4.6 \text{ deg}^2$  (*YJHK<sub>s</sub>*) of the UltraVISTA and VIDEO data sets (McCracken et al. 2012; Jarvis et al. 2013) centred at RA 10h and DEC  $2.2^\circ$  for D10 and RA 2.2h and DEC  $-4.5^\circ$  for D02 (Davies et al., in preparation). The imaging data sets in *ugrizYJHK<sub>s</sub>* filters come from the following sources: the *u* band originates from the CFHT, the *griz* bands from the Hyper Suprime Camera Strategic Program (HSC; Aihara et al. 2018), and the *YJHK<sub>s</sub>* bands from either UltraVISTA-DR3 or VIDEO XMM-LSS. For more detail on the photometric catalogue, see the DEVILS photometry description paper (Davies et al., in preparation). In the same manner as the updated GAMA photometry, the photometric catalogue has also recently been reassembled using the PROFOUND source finding analysis package from the FUV to FIR (Davies et al., in preparation).

Improvements over previous photometry include those highlighted for GAMA through the use of PROFOUND, bringing consistency of methodology, with comparable levels of visual checks and manual fixes.

### 2.3 Hubble Space Telescope and other deep data

For the deepest data, we adopt the deep number counts from Driver et al. (2016b), which were mostly obtained from the *HST*, Wide Field Camera 3 (WFC3) Early Release Science (ERS) archive (WFC3-ERS; Windhorst et al. 2011) in combination with the *HST* Ultra-Violet Ultra-Deep fields (UVUDF; Teplitz et al. 2013). The data reduction of the panchromatic WFC3 ERS filters are discussed in Windhorst et al. (2011). They derived deep field galaxy number counts across the WFC3 ERS filters (F336W, F435W, F606W, F775W, F850LP, F098M, F125W, and F160W) from *u* band to *Y* band. The panchromatic photometric counts for the same filters from NUV to NIR in the Hubble Ultra Deep Field (HUDF) are described in Rafelski et al. (2015).

We note that other *HST* fields exist, however, we have chosen to exclusively use the ERS and UV-UDF data as they have independent detections in each band, thereby circumventing the colour bias that is introduced through forced aperture photometry. We note that a full reanalysis of the entire ACS WFC3 archive is currently underway, as part of the SkySURF *HST* Legacy Program (PI: Windhorst), and

**Table 1.** A summary of multiwavelength data used in this analysis. The reference surveys for the analysis are as follows: GAMA (Bellstedt et al. 2020a); DEVILS (Davies et al., in preparation); *HST* ERS Data 3 and UVUDF (Grazian et al. 2009; Windhorst et al. 2011; Fontana et al. 2014; Rafelski et al. 2015). The pivot wavelength refers to the GAMA data.

EBL Filter	Survey			EBL Pivot Wavelength ( $\mu\text{m}$ )	Depth ( $5\sigma$ AB)	
	GAMA	DEVILS	<i>HST</i> +		GAMA	DEVILS
<i>u</i>	VLT KiDS	CFHT( <i>u</i> <sup>*</sup> )	F336W, LBT <sup>a</sup> U360 <sup>b</sup>	0.3577	24.3	26.4
<i>g</i>	VLT KiDS	HSC <sup>c</sup> <i>g</i>	F435W	0.4744	25.1	27.3
<i>r</i>	VLT KiDS	HSC <i>r</i>	F606W	0.6312	24.9	26.9
<i>i</i>	VLT KiDS	HSC <i>i</i>	F775W	0.7584	23.8	26.7
<i>Z</i>	VISTA VIKING	HSC <i>z</i>	F850LP	0.8833	23.1	26.3
<i>Y</i>	VISTA VIKING	UltraVISTA	F098W, F105W	1.0224	22.3	24.7
<i>J</i>	VISTA VIKING	UltraVISTA	F125W	1.2546	22.1	24.5
<i>H</i>	VISTA VIKING	UltraVISTA	F160W	1.6477	21.5	24.1
<i>K<sub>s</sub></i>	VISTA VIKING	UltraVISTA	ESO K <sup>d</sup>	2.1549	21.2	24.5

<sup>a</sup>Large Binocular Telescope (LBT).

<sup>b</sup>Large Binocular Camera (LBC).

<sup>c</sup>Hyper Suprime Camera (HSC).

<sup>d</sup>European Southern Observatory (ESO/VLT/Hawk-I).

the inclusion of additional *HST* fields in IGL EBL analysis will be the subject of a future paper.

In the *u* band, we retain the LBT data from Grazian et al. (2009) and in the *K<sub>s</sub>* band we also retain the deep data from Fontana et al. (2014) using ESO VLT Hawk-I with an exposure time of 13 h, and reaching a depth of 27.3 AB magnitude ( $1\sigma$  limit).

Table 1 summarizes the wavelength coverage and depth of data used in this work.

## 2.4 Colour transformations

The data sets described above come from a variety of facilities with aligned but slightly differing filters and facility throughput transmissions. To derive galaxy number counts across consistent bands, we need to implement colour transformations to a common filter set. Here, we elect to use the VST *ugri* and VISTA *ZYJHK<sub>s</sub>* filters as our EBL reference filters. The transformations we need include the DEVILS optical data (CFHT *u*<sup>\*</sup> and HSC *griz* filters), all *HST* data (F336W, F435W, F606W, F775W, F850LP, F098W, F105W, F125W, and F160W), the LBT data (U360 filter), and the ESO Hawk-I (*K<sub>s</sub>* filter). For the DEVILS data, we have full access to the flux measurements for each individual galaxy through our segment-matched PROFOUND photometry. Hence, we can convert robustly from native to KiDS filters, by including a colour term to fold in the second-order dependence on the spectral shape. For the *HST* + data sets, we only have access to the number-count data, which have mostly been determined independently in each band, and hence can only determine a mean first-order filter offset given some reasonable assumption as to the likely mean spectral shape and redshift distribution of the underlying galaxy population (see also the discussion in Windhorst et al. 2011).

To determine our filter transformations, we use the PROSPECT package (Robotham et al. 2020) to generate several thousand galaxy spectra with a uniform redshift distribution from  $z = 0$  to  $z = 2$ , and using the PROSPECT default metallicity, dust properties, a Chabrier IMF (Chabrier 2003), and a randomly selected star formation history (SFH). We then determine the fluxes for these spectra as observed through our reference filters and through the filters for each of the data sets we wish to transform. We fit for the difference between the measured fluxes in the original and target filters, with a linear dependence on the colour term for DEVILS, and without a colour

**Table 2.** Filter transformations used to place all data on to the VST/VISTA filter systems (i.e. *ugriZYJHK<sub>s</sub>*) using our online tool at: <https://transformal.cicar.org>.

Filter transformation	Intrinsic Uncertainty
$u_{\text{VST}} = u_{\text{CFHT}}^* + 0.2828(u_{\text{CFHT}}^* - g_{\text{HSC}}) - 0.0344$	0.056
$g_{\text{VST}} = g_{\text{HSC}} + 0.0331(g_{\text{HSC}} - r_{\text{HSC}}) + 0.0163$	0.017
$r_{\text{VST}} = r_{\text{HSC}} - 0.0433(g_{\text{HSC}} - r_{\text{HSC}}) + 0.0012$	0.010
$i_{\text{VST}} = i_{\text{HSC}} + 0.0549(r_{\text{HSC}} - i_{\text{HSC}}) + 0.0073$	0.006
$Z_{\text{VISTA}} = z_{\text{HSC}} + 0.0538(i_{\text{HSC}} - z_{\text{HSC}}) + 0.0037$	0.007
$u_{\text{VST}} = U360_{\text{LBT}} + 0.0038$	0.006
$u_{\text{VST}} = F336W_{\text{HST}} - 0.113$	0.089
$g_{\text{VST}} = F435W_{\text{HST}} - 0.159$	0.112
$r_{\text{VST}} = F606W_{\text{HST}} - 0.114$	0.070
$i_{\text{VST}} = F775W_{\text{HST}} + 0.031$	0.019
$Z_{\text{VISTA}} = F850LP_{\text{HST}} + 0.057$	0.049
$Y_{\text{VISTA}} = F098W_{\text{HST}} - 0.076$	0.053
$Y_{\text{VISTA}} = F105W_{\text{HST}} + 0.066$	0.078
$J_{\text{VISTA}} = F125W_{\text{HST}} - 0.015$	0.022
$H_{\text{VISTA}} = F160W_{\text{HST}} - 0.066$	0.024
$K_{\text{SVISTA}} = K_{\text{SHawk-I}} + 0.000$	0.002

term for the *HST* + data. As part of the fitting process, we determine an estimate of the intrinsic uncertainty in the transformation process, which will of course be higher for the *HST* + data sets (because we lack the colour terms). We note that in the future we are looking to reprocess the entire *HST* archive as part of the SKYSURF *HST* Archival program (PI: R. Windhorst), which will allow us, in due course, to factor in the proper *HST* colour terms. Table 2 shows the resulting transformations for the filters used in this work which we now apply.

## 3 RESULTS

### 3.1 Number counts

Fig. 1 shows our revised galaxy number count compilations in *ugriZYJHK<sub>s</sub>* bands as derived from the deep and wide data (GAMA, DEVILS, and *HST* +). Fig. 2 shows the same data, but with a linear term of  $d(\log_{10}(N))/dm = 0.4$  removed to (a) highlight discrepancies; and (b) highlight the contribution of each magnitude interval to the



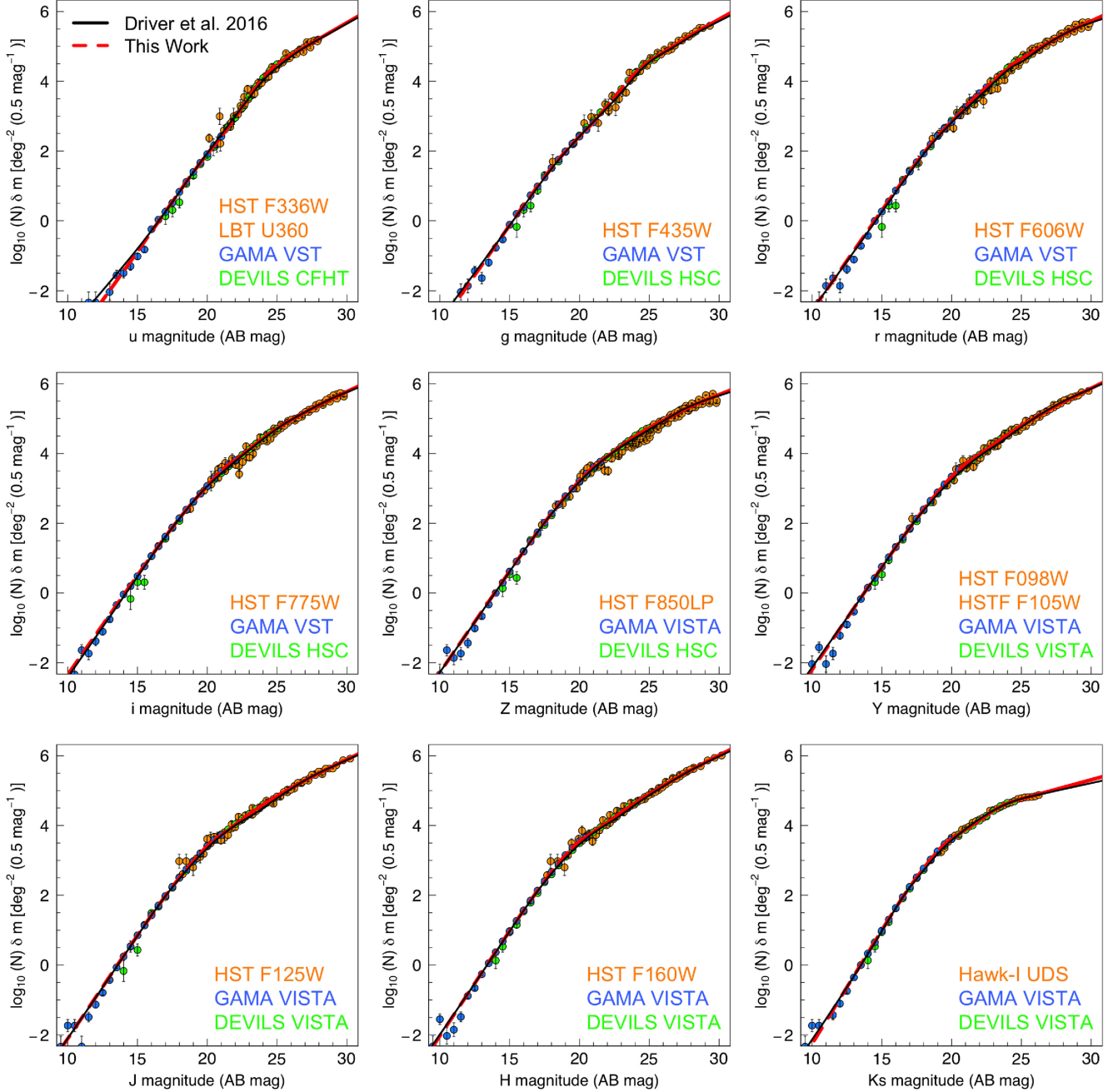


**Figure 1.** The galaxy number count in each filter for a combination of data sets derived from the GAMA, DEVILS, and the *HST* surveys in blue, green, and orange, respectively. We fitted a smooth spline in a red dashed line through all data sets. For a sanity check, we compare to published data (Driver et al. 2016b). The black solid line shows a fit to their data. The error bars indicate the Poisson error.

final EBL. The IGL is simply the integral under these data. In both figures, the number counts are in units of magnitudes per 0.5 mag interval per square degree, and the uncertainties shown are based purely on Poisson statistics. From the observational point of view, the IGL derives as below

$$\text{IGL} \propto \int N_m \times 10^{-0.4-m} dm. \quad (1)$$

Where  $N$  is the number of galaxies per magnitude bin between  $m$  and  $m + \delta m$ .

Each data set is truncated at the faint end at the point at which it becomes inconsistent with deeper data (see Fig. 1). As can be seen, the overlap between the data sets is smooth, with no obvious discontinuities. As a result, the galaxy number counts indicate good agreement in all bands with the largest discrepancies seen in the  $u$  and  $g$  bands where more robust Galactic extinction corrections may become important (in terms of both spatial distribution and reddening). Driver et al. (2016b) discussed possible sources of both systematic and statistical error. These will be discussed in more detail in Section 4.

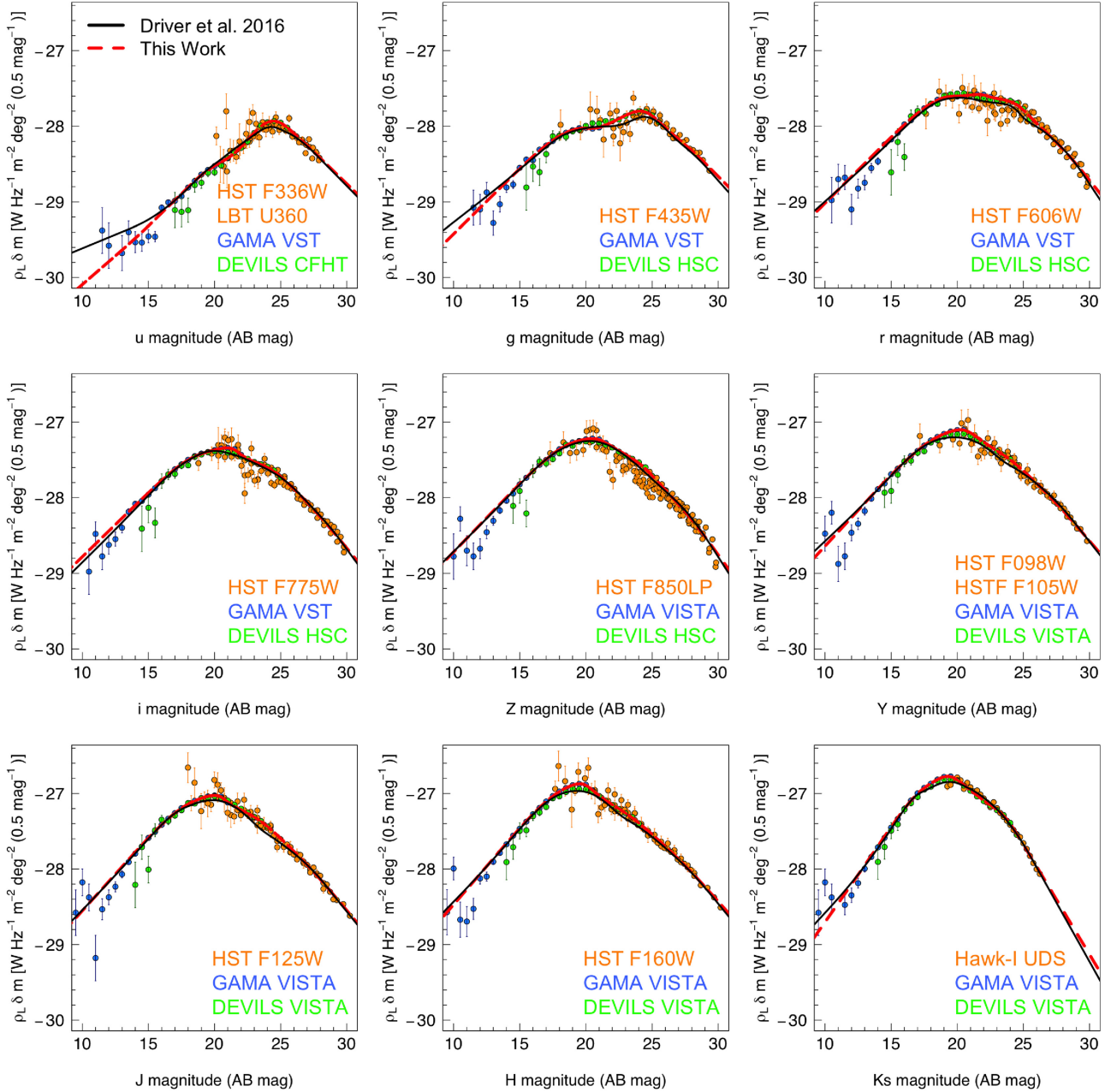


**Figure 2.** The contribution of each magnitude bin to the energy density. The count has been normalized and scaled for each survey in depth and area.

Fig. 2 shows the same plot but now in terms of the differential luminosity density contribution from each magnitude interval. Hence it is the integral under this curve that provides the final EBL measurement in that band. Fig. 3 shows the cumulative version of the same plot.

### 3.2 Extragalactic background light

In order to estimate the total EBL from discrete sources in each band, we fit a smooth spline with 10 degrees of freedom ( $df = 10$ ) to the combined luminosity density data, inverse weighted by the variance. We then integrate the spline fit from  $-100$  to  $+100$  AB magnitude. Assuming no unexpected behaviour of the spline outside the data range, Fig. 2, shows the contribution of each magnitude bin to the EBL in all filters (as indicated) in the unit of  $\text{W Hz}^{-1} \text{m}^{-2}$  per 0.5

magnitude bin, and normalized by effective area. As ought to be expected, the contribution to the IGL is limited at both very faint and very bright magnitudes with most of the EBL contribution coming from intermediate magnitudes (and redshift). Following integration we convert to the standard EBL units using equation (2).

$$\text{EBL} = u \times 3282.1 \times 10^9 \times (c/\lambda), \quad (2)$$

where  $u$  is the energy density,  $c$  is the speed of light in  $\text{m/s}$ , and  $\lambda$  is the wavelength in metres, and the constant converts the measurements into units of  $\text{nW m}^{-2} \text{sr}^{-1}$ . Note that the fraction of the IGL in the extrapolated of the spline fit is typically less than a few per cent, see Fig. 3.

Fig. 2 shows the luminosity density with the spline fits overlaid (red dashed line) for each band. We compare our best-fitted splines in red dashed lines to the compendium of Driver et al. (2016b) shown

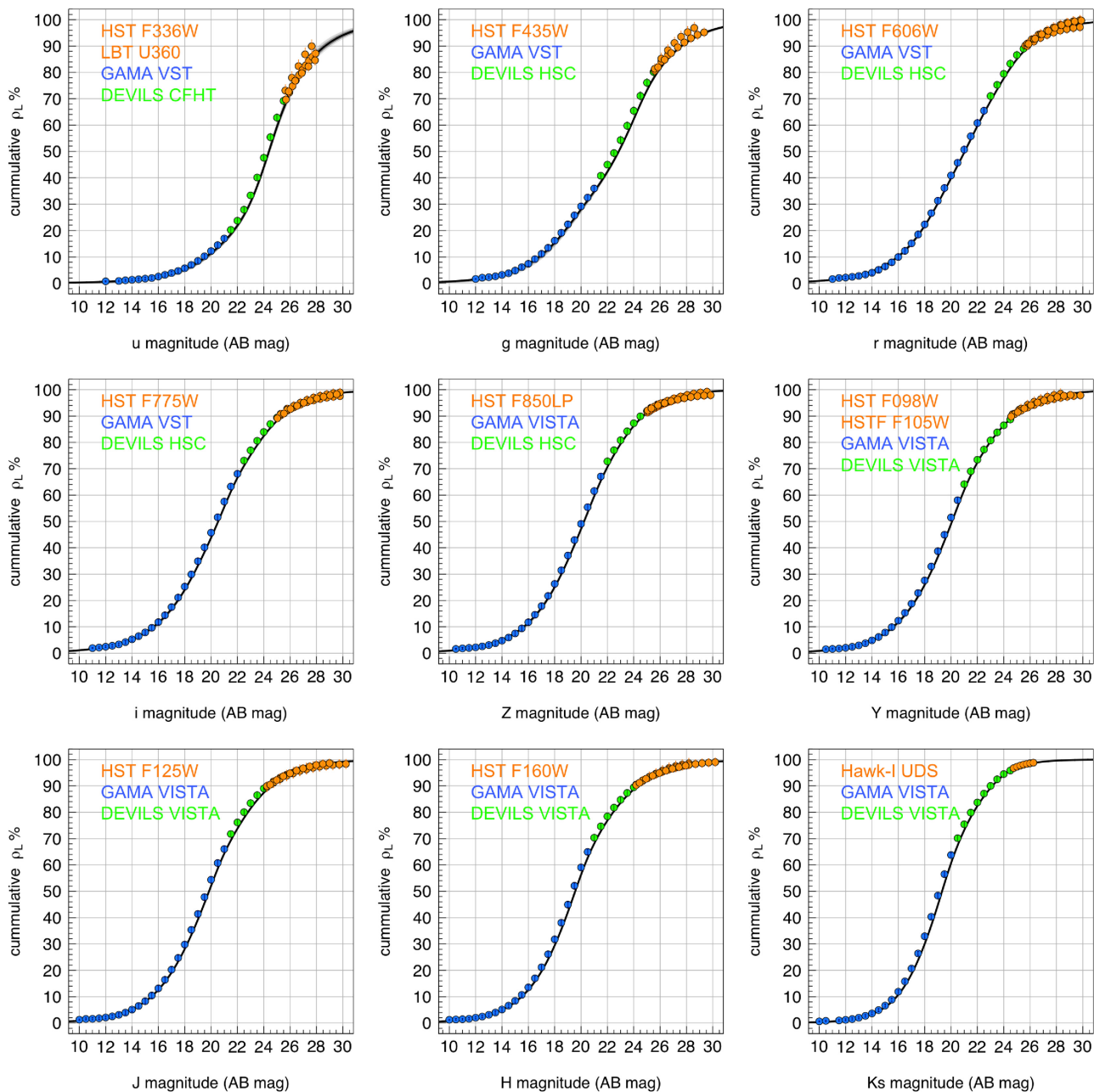


**Figure 3.** The cumulative contribution function ( $\rho_L$ ) to each band.

as solid black lines. Our data are clearly bounded at both ends in all filters and show a well-defined peak at intermediate magnitude levels in all bands.

#### 4 ERROR ESTIMATES

In this section, we explore error estimation taking into consideration the systematic and random errors for each band. Our systematic errors break down into cosmic variance (CV) and zero-point (ZP) uncertainty, while random errors are due to Poisson error, as well as the uncertainty inherent in the fitting process. The final uncertainty is then the combination of these four separate errors, which we explore in a full Monte Carlo (MC) analysis. Below we discuss each of

these individually to address their impact on our final EBL COB measurements.

##### 4.1 Poisson error

To estimate the impact of Poisson uncertainty alone, we performed an MC analysis with 1001 iterations. Within each iteration, we perturb the galaxy number-counts by their associated density uncertainty error, and repeat our full analysis. For the perturbation of each data point, we sample a Gaussian distribution with mean zero and a standard deviation equivalent to the quoted number-count error for that magnitude bin. The top row of Fig. 4 shows a range of the MC fits (left-hand panel), and the recovered IGL measurement (right)

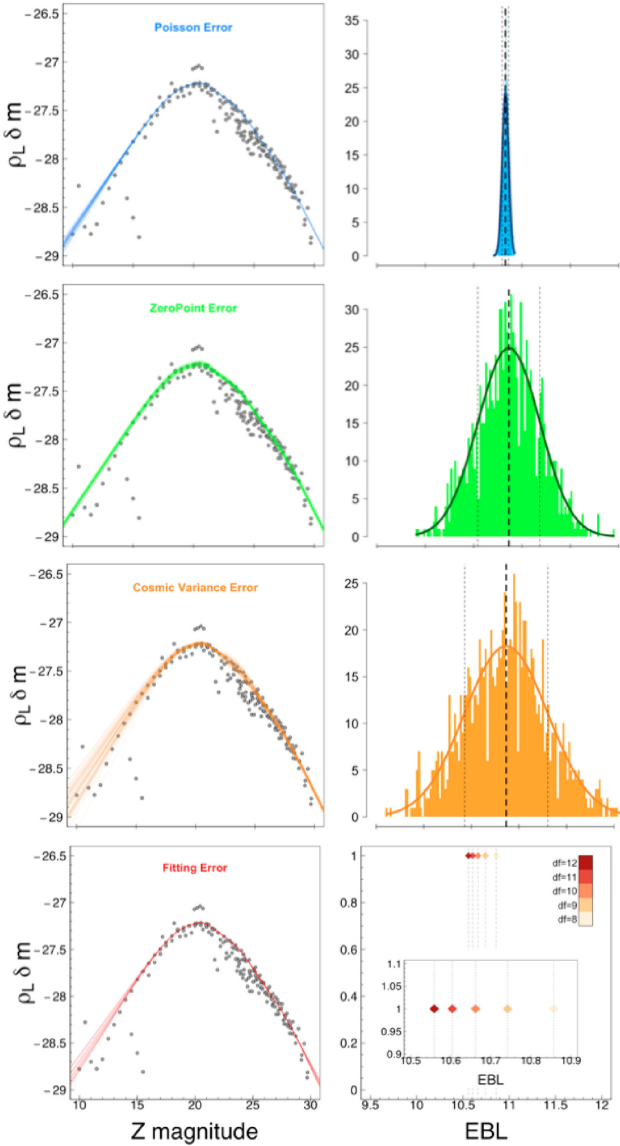


**Figure 4.** An example of a luminosity density plot including all possible sources of error including the Poisson, CV, ZP, and fitting in blue, orange, green, and red for the Z band, respectively. Left column shows the contribution of each uncertainty to the EBL. Right column shows the distribution of our IGL for each source of error. The mean and standard deviation ( $1\sigma$ ) are shown in black and grey solid lines, respectively.

for 1001 realizations in the Z-band. From this we determine a mean value of 10.658 and a standard deviation of 0.035 i.e.  $< 1$  percent error. Table 3 shows this estimate due to Poisson error from  $u$  to  $K_s$  and in general this error is fairly negligible throughout, as expected given the large sample size.

#### 4.2 Zero-point error

Errors in the absolute zero-point calibration will also affect the number-counts in a systematic manner for a given data set, but randomly between the data sets, and randomly between filters. Here, we estimate the zero-point errors in the GAMA/KiDS data by comparing the KiDS/VIKING photometry to the SDSS/2MASS

photometry, incorporating appropriate filter conversions as provided by Kuijken et al. (2019) for KiDS (only relevant for  $u$  and  $r$  band, see their fig. 5 and equation 5), and González-Fernández et al. (2018) for VISTA (in  $ZYJHK_s$  bands, see their equations 5–9 and also appendices A and C). In effect, we are attempting to provide an independent albeit basic calibration check of the KiDS and VIKING data, compared to the more sophisticated calibration conducted by the KiDS and VISTA CASU (Cambridge Astronomy Survey Unit) teams. The zero-point verification analysis is done on a square-degree by square degree (i.e. TILE) basis, and we exclusively use stars in a restricted magnitude range, where bright stars are not saturated in KiDS/VIKING, and faint stars are not dominated by sky noise for SDSS/2MASS. Left-hand panel in Fig. 5 shows an example comparison for the  $ugriZYJHK_s$  filters for a single TILE centred at  $RA = 8.5h$  and  $Dec = -0.5^\circ$ , the yellow data points highlight the magnitude range used, while the grey data points showing the full range of the comparison. From the yellow data points, we determine a simple offset and a linear fit for each filter and for each TILE, as indicated by the cyan and mauve lines, respectively. In general, the fits are good, showing relatively little magnitude dependence, and hence we use the simple offsets as our indicator of the zero-point offset for each TILE. Fig. 5 (right) shows the histogram of these zero-point offsets for the 220 TILES that make up the GAMA KiDS/VIKING data set reflecting a distribution of zero-point uncertainty. For each filter, we determine the median absolute zero-point offset, and the  $1\sigma$  zero-point uncertainties from a simple Gaussian fit, and the empirical standard deviations (as indicated in the Figure panels). We also note that the KiDS team identified a Galactic Latitude dependency of  $-0.02$  to  $0.1$  mag in the  $u$  band, potentially explaining the much broader spread that we see here. We also note that the VISTA zero-points evolved from VISTA reduction 1.3 to 1.5 with implied zero-point changes of  $-0.03$ ,  $0.018$ ,  $-0.0200$ ,  $0.0067$ , and  $0.0106$ , for the five VISTA bandpasses ( $ZYJHK_s$ ), respectively (see González-Fernández et al. 2018, appendix D). We therefore elect to adopt worst case scenario for the zero-point errors by combining all of the uncertainties in quadrature [i.e. literature offset + median offset + ( $1\sigma$ ) spread + intrinsic uncertainty from Table 2] to obtain ultra-conservative zero-point uncertainties of: 0.11, 0.022, 0.011, 0.018, 0.041, 0.021, 0.032, 0.022, and 0.037 for the GAMA  $ugriZYJHK_s$ , respectively.

For the DEVILS and *HST*+ data sets, we adopt the zero-point uncertainties as the maximum of either those found for GAMA, or an error floor of 0.03 mag for DEVILS (i.e. that adopted in D18) or *HST*+. In addition, we also fold into the DEVILS and *HST*+ zero-point errors the intrinsic uncertainty from the filter transformations shown in Table 2. Technically, this overestimates the likely colour transformation error (as it will be random not systematic), but this is a convenient place to incorporate it that errs on the side of caution. Table 4 shows the final adopted zero-point errors for each data set and each band.

With conservative zero-point errors in hand, we can now MC simulate the impact of the zero-point error by perturbing the magnitudes for each of our three data sets (GAMA, DEVILS, and *HST*) in a systematic manner, but independently for each data set and for each filter. To do this, we draw a random value for each data set and filter from a Gaussian distribution with a mean of zero and a standard-deviation defined by the relevant zero-point uncertainty (Table 4), and systematically adjust the magnitude bins of each survey by this amount for that filter. Finally, we refit our splines and re-derive our optical/NIR IGL measurements 1001 times to build up a distribution of the impact of the zero-point errors. The results are shown in Table 3 and Fig. 4.



**Table 3.** Integrated EBL results considering individual errors. Column 2 shows our IGL measurement in each band. Columns 3 to 6 show the mean offset in per cent for the contribution of each uncertainty. Finally, column 7 presents the total error (added in quadrature) as a percentage of the IGL.

Filter	EBL ( $\text{nW m}^{-2} \text{sr}^{-1}$ )	Poisson error (per cent)	Cosmic variance Error (per cent)	Zero-point Error (per cent)	Fitting error (per cent)	Total (per cent of IGL)
u	4.13	0.38	2.54	6.36	0.35	6.87
g	5.76	0.49	3.29	2.07	0.92	4.02
r	8.11	0.37	3.55	1.44	1.34	4.08
i	9.94	0.35	3.98	1.67	0.99	4.44
Z	10.71	0.30	3.98	3.16	1.06	5.20
Y	11.58	0.32	4.11	1.62	0.88	4.52
J	11.22	0.29	4.25	2.35	0.75	4.92
H	11.17	0.26	4.38	1.63	0.65	4.73
Ks	9.42	0.19	4.12	3.09	0.74	5.21

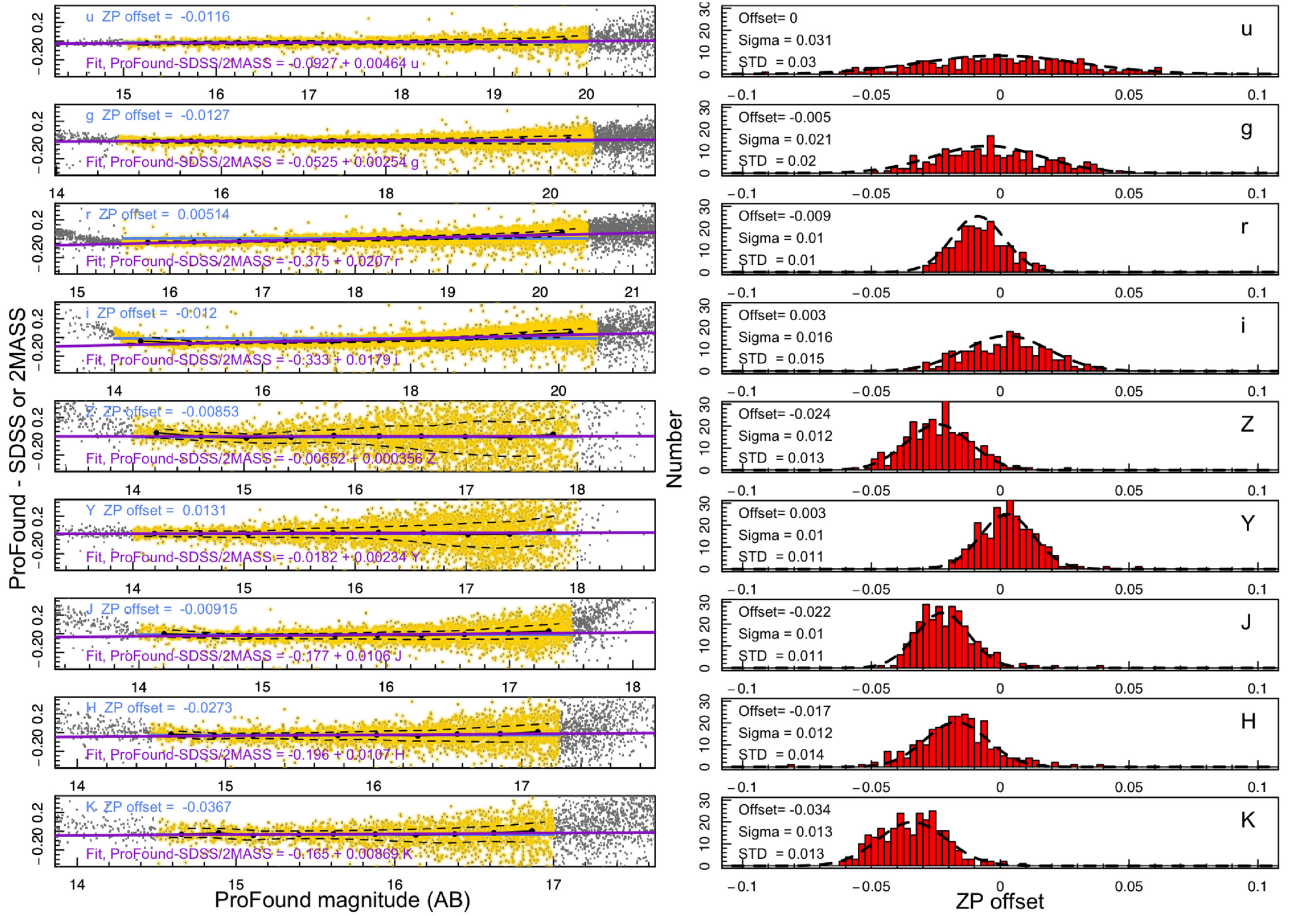


**Figure 5.** Left-hand panel: A direct comparison of the GAMA PROFOUND photometry to either SDSS (*ugriZ*) or 2MASS (*YJHK<sub>s</sub>*) data, using objects classified as stars. The region we use for determining offsets for each TILE and for each filter are shown in yellow, with the offsets and line fits for each sample shown in blue or mauve, respectively. Right-hand panel: the compendium of zero-point offsets for all 220 TILES with the  $\sigma$  of the Gaussian fit and the standard deviation shown on each panel.

**Table 4.** Adopted zero-point uncertainties for each data set and each filter.

Data set	<i>u</i>	<i>g</i>	<i>r</i>	<i>i</i>	<i>Z</i>	<i>Y</i>	<i>J</i>	<i>H</i>	<i>K<sub>s</sub></i>
GAMA	0.11	0.02	0.01	0.02	0.04	0.02	0.03	0.02	0.04
DEVILS	0.11	0.03	0.03	0.03	0.04	0.03	0.03	0.03	0.04
HST+	0.11	0.08	0.13	0.06	0.04	0.04	0.07	0.03	0.04

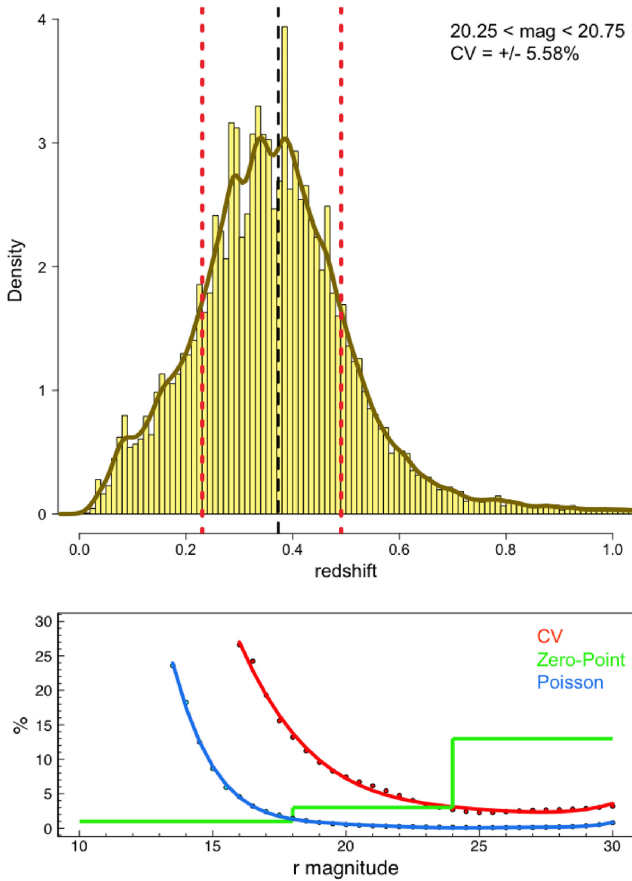


**Figure 6.** Top panel: CV density distribution for a sample of a magnitude bin in the  $r$  band. The dashed black line denotes the mean redshift. Upper/lower quantiles are displayed in dashed red lines. Bottom panel: The CV compared to the zero-point and Poisson uncertainties.

### 4.3 Cosmic variance error

Pragmatically, CV can be considered as a systematic uncertainty inherent in observational estimates of the volume of the extragalactic sky due to large-scale density fluctuations. This error is quite significant in most galaxy surveys, and is often the dominant error in measuring the IGL (especially in deep galaxy surveys).

For the GAMA survey, we obtained a mock catalogue using the SHARK semi-analytical model of galaxy formation and evolution (Lagos et al. 2019; Bravo et al. 2020) used to construct light-cones for the GAMA regions. To estimate our CV error, we can determine the effective volume from the 16 percent and 84 percent quantiles of the predicted redshift distribution,  $n(z)$ , for the magnitude slice in question, and evaluate equation 3 from Driver & Robotham (2010). We use an effective sky area of  $60 \text{ deg}^2$ , redshift ranges of the comoving cone, and set the number of separated regions to 4 for each survey to obtain the CV error. Top panel in Fig. 6 shows an example redshift distribution for the magnitude range of  $20.5 \pm 0.25$  in the  $r$  band. Fig. 6 (bottom panel) also highlights the variation of the CV as a percentage (solid red line) compared to the zero-point (solid green line) and Poisson (solid blue line) uncertainties.

For the DEVILS/D10 + D02 and *HST* surveys, we also adopted the CV uncertainty following equation 3 of Driver & Robotham (2010) for the appropriate sky area for the particular survey, and adopting an approximate redshift range. To determine the approximate redshift ranges to use for the DEVILS/D10 + D02 and *HST* surveys, we

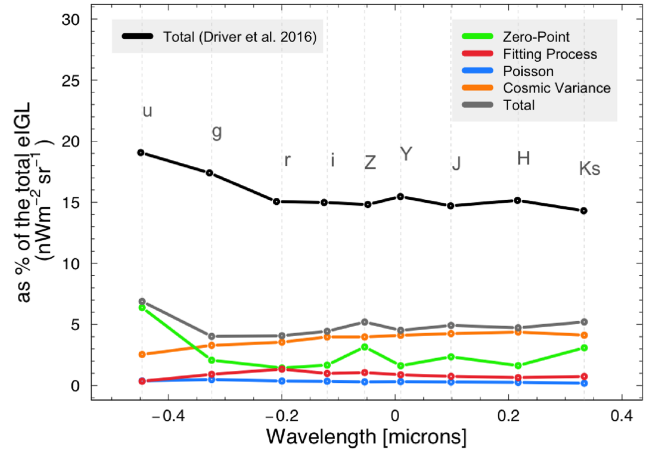


**Figure 7.** A contribution of each systematic and random uncertainties to the IGL for each filter. The contribution of the CV to the IGL is dominant across the optical and NIR filters. Random errors have an insignificant contribution to the IGL estimation. Our total error (in grey line) has been compared to Driver et al. (2016b) marked with black line.

sliced a mock galaxy catalogue generated by the SHARK team into the 16 percent and 84 percent quantile ranges independently for each magnitude bin and each bandpass. For our three data sets, we then calculated CV fluctuations for each magnitude bin, and perturb the galaxy counts in the magnitude direction using this value for each filter and independently for each data set. We perform an MC simulation with 1001 iterations and, consequently, rederived the IGL EBL. Throughout the CV analysis, the procedure was forced to start from the same random seed to ensure that the CV error is correlated across the filters. Table 3 shows the error from the CV.

### 4.4 Fitting error

To calculate the IGL, we performed a spline fit using an arbitrarily selected 10 degrees of freedom. Fig. 4 (lower) shows the shift in the Z band IGL value if we use a spline of order 8, 9, 10, 11, or 12. On the whole, the shift is marginal, as compared to that from the Poisson error (see top panel in Fig. 4), and far less than the effect of either CV or the zero-point errors.

### 4.5 Final error

Table 3 summarizes the integrated EBL results showing the individual errors. Fig. 7 shows the contribution of each error as a percentage of the optical/NIR IGL in a single graph. We show the photometric, spline fitting, Poisson, and CV error in green, red, blue, and orange lines, respectively. As can be seen, the systematic CV and zero-point errors dominate for all filters, while the contribution of random errors (fitting and Poisson) is negligible. The solid line also highlights the total error budget for all optical and near-IR filters ( $ugriZYJHK_s$ ) comparing to the previous result from Driver et al. (2016b); shown as a black line.

We finally combine the errors in quadrature, to produce our final IGL error estimates. However, we note that the errors are a mixture of both random and systematic errors. Table 3 (last column) shows our final error estimate as a percentage of the IGL value. As a consequence of the revised data, colour transformations and revised error analysis, the IGL error, compared to the earlier results of Driver et al. (2016b), is reduced from  $\sim 20$  percent to the mean error of  $\sim 8$  percent.

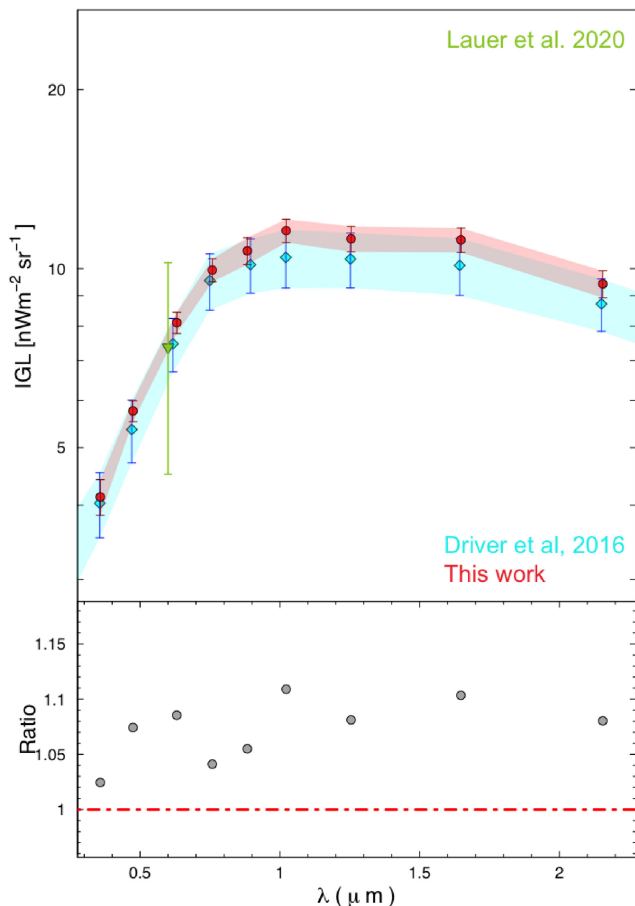


**Figure 8.** Top panel: The IGL as a function of wavelength estimated in Driver et al. (2016b) and this work marked with cyan diamonds, and red circles, respectively. Shaded areas correspond to the total error. For comparison, we show the IGL estimate from Lauer et al. (2021) as a lower limit. As can be seen, their estimate is consistent with our measurement. Bottom panel: The ratio of IGL measured in this work to the IGL measured by Driver et al. (2016b). The red dot-dashed line corresponds to the equality line between the two measurements.

## 5 COSMIC OPTICAL BACKGROUND RESULT

### 5.1 Comparison to previous IGL data

The top panel in Fig. 8 shows the comparison between our new IGL measurements and the results from Driver et al. (2016b), who used essentially the same methodology, but which we have improved by the replacement of SDSS data with VST KiDS data, a full reanalysis of the core GAMA and COSMOS/DEVILS number-counts data, as well as an improved error analysis. We also include the very recent data from the New Horizons LORRI (Lauer et al. 2021) using the Zemcov et al. (2017, green triangle) estimates that were obtained at an even greater distance of  $> 40$  au from the Sun. The data are obtained at the LORRI pivot wavelength of  $0.608 \mu\text{m}$  at high galactic latitude after subtracting estimates of the outer Kuiper belt light and DGL. The Lauer et al. (2021) IGL estimate is measured as  $7.37 \pm 0.81 \pm 2.05$  (random and systematic errors, respectively)  $\text{nW m}^{-2} \text{sr}^{-1}$ , which looks consistent with an interpolation of our IGL points at 0.6 microns.

The ratio of our revised measurement of the IGL for each filter, to that from Driver et al. (2016b) is shown in the lower panel of Fig. 8, and highlights the changes resulting from the current analysis. As the areas covered by the contributing surveys are essentially identical, the reduction in error comes mainly from the improvement in our modelling of the CV, which now relies on the SHARK galaxy formation simulations (see Lagos et al. 2019), and improved colour corrections (see Robotham et al. 2020). In all wavebands, we see modest increase in the recovered IGL value of approximately 5–15 per cent (see lower panel of Fig. 8). While in all bands the change is within the errors, it is systematic across the filters. We believe this is due to a combination of PROFOUND recovering more accurate total fluxes than the previous source detection algorithms (see fig. 14 in Robotham et al. 2018), the improved depth of KiDS over SDSS, improved star–galaxy separation (see Bellstedt et al. 2020a), and to a lesser extent more accurate accounting of the masked area, i.e. that lost near bright foreground stars. We note that this increase in the IGL measurements brings into line the IGL and the VHE data, available at that time, in which Driver et al. (2016b) noted a 10–20 per cent discrepancy. At the time, this was tentatively attributed to the possibility of stripped mass (e.g. ICL and Intra-Halo Light) and/or missing populations. See also all discussion in Ashcraft et al. (2018). They found  $\leq 10$ –20 per cent of light to surface brightness  $\sim 32$  mag.

### 5.2 Comparison to very high-energy constraints

As indicated in the introduction, VHE studies estimated the EBL intensity through the production of electron–positron pairs as a by-product of the interaction of high energy photons, emanating from the distant blazars, with micron wavelength photons in the EBL. This interaction results in the decrement of the expected power-law distribution of high energy photons with 100 GeV blazar photons preferentially interacting with micron wavelength EBL photons. At present, most VHE applications require an input EBL model curve and constrain the normalization of the curve. Fig. 9 presents the most recent results from FL18, who studied 759 active galaxies as observed via the Fermi Large Area Telescope (LAT). In Fig. 9, we compare our new IGL measurements to published VHE COB measurements (Biteau & Williams 2015; Ahnen et al. 2016; FL18; HESS Collaboration 2018). This latest result shows full consistency with our optical/NIR IGL data, however, we note that an improved comparison could be made by a re-analysis of the VHE data that adopts an EBL model fitted to our IGL data (see Section 6).

Current attempts, within the VHE community, are now ongoing to not only constrain the EBL normalization, but also the shape of the EBL COB SED (see e.g. Abeysekara et al. 2019). Recently, the VERITAS team (Biteau & Williams 2015) demonstrated this by detecting and measuring the spectra of 14 blazars at VHE ( $> 100$  GeV) in order to enable a full reconstruction of the SED of the EBL. However, at this stage, the analysis errors are too large to be useful.

The shaded area obtained by the VHE COB measurement also depicts the range of the allowed EBL intensity in the optical/near-IR filters (from  $0.24 \mu\text{m}$  to  $4.25 \mu\text{m}$  for MAGIC and extending to  $10.4 \mu\text{m}$  for H.E.S.S.). At this stage, it can only really be stated that the VHE data are fully consistent with our IGL measurements in the  $u - K_s$  range without the need to include any significant additional source of diffuse light.

As the errors in both the optical/NIR IGL and VHE COB data improve to the few per cent level, the comparison between these



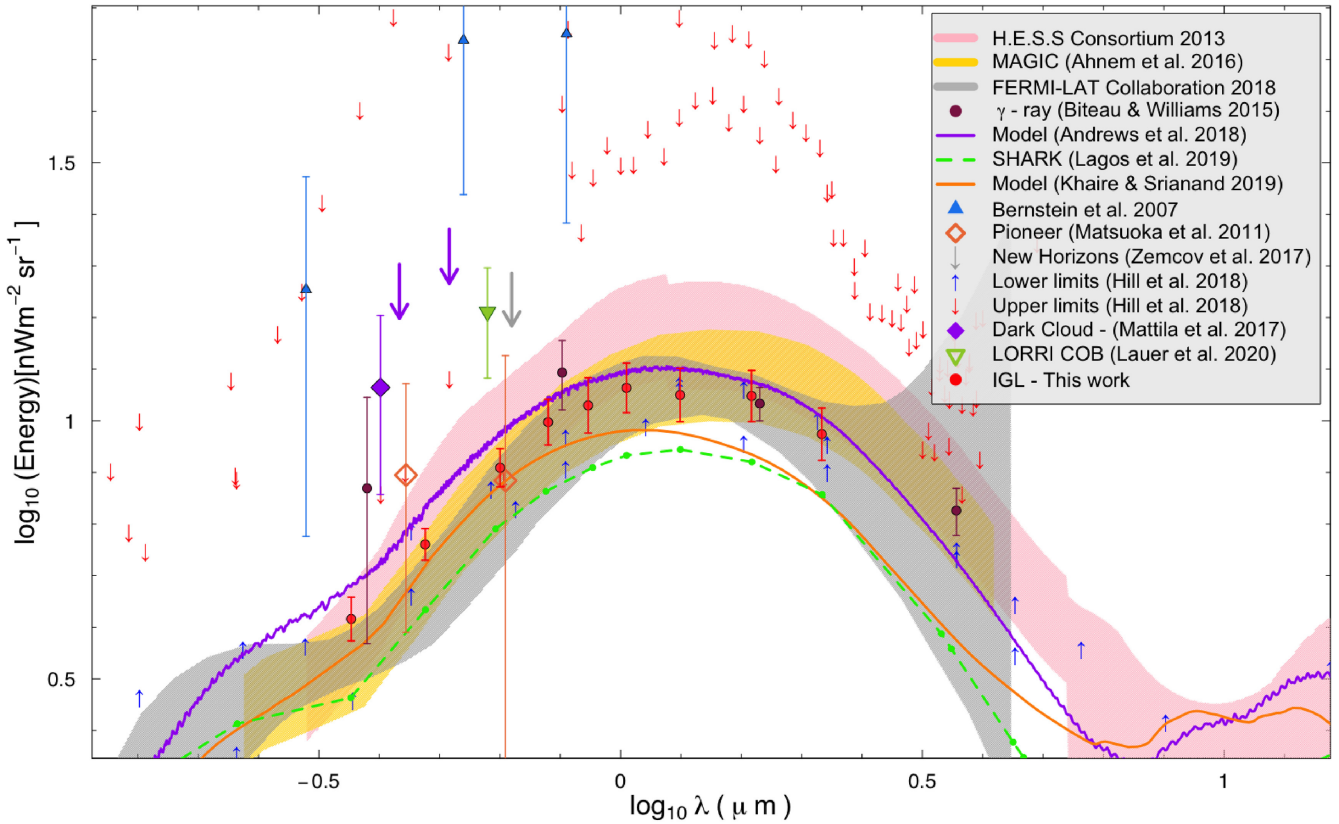


**Figure 9.** Our measurement of the IGL based on galaxy number counts from wide and deep surveys (GAMA+DEVILS + *HST*) in nine multiwavelengths from  $u$  to  $K_s$  band (red circles). We compared our IGL to literature measurements taken from various techniques. Direct estimates: (Bernstein 2007) in blue triangles; New Horizons (Zemcov et al. 2017) as an upper limit in grey; Pioneer 10/11 (Matsuoka et al. 2011) in orange diamonds; recent estimates from the New Horizons LORRI (Lauer et al. 2021) in green triangle. VHE estimates: (MAGIC Collaboration 2008) in yellow shades; (HESS Collaboration 2018) in pink shades; (FL18) in grey shades;  $\gamma$ -ray observation from Biteau & Williams (2015) in violet circles. Dark Cloud: (Mattila et al. 2017a) and upper limits in purple. We also compared the EBL estimation obtained from the models: SHARK (Lagos et al. 2019) green dashed line; (Khair & Srikanth 2019) orange line; GAMA (Andrews et al. 2018) purple line. Finally, we added a data assembled by Hill et al. (2018) from radio to  $\gamma$ -ray wavelengths as an upper and lower limit following by the red and blue arrows, respectively.

complementary methods should provide interesting constraints on the presence, or lack of non-bound optical/NIR emission.

### 5.3 Comparison to direct EBL constraints from space platforms

Fig. 9 shows a comprehensive compilation of nearby Solar system measurements of the COB. These mainly stem from direct background measurements of *HST* data, and are often shown as either upper limits (Bernstein 2007) or sometimes shown as tentative measurements (Hill et al. 2018). The open orange diamonds and grey square show direct estimates from the Pioneer 10/11 (Matsuoka et al. 2011) and New Horizons (Zemcov et al. 2017) spacecraft at distances  $> 4.5$  au, respectively. Pioneer 10/11 reported measurement of the reanalysed EBL beyond 4.5 au as  $7.9^{+4.0}_{-4.0}$  and  $7.7^{+5.8}_{-5.8}$   $\text{nW m}^{-2} \text{sr}^{-1}$  at 0.44 and 0.64  $\mu\text{m}$ , respectively. New Horizon also reported the EBL as  $4.7^{+7.3}_{-7.3}$   $\text{nW m}^{-2} \text{sr}^{-1}$  at 0.66  $\mu\text{m}$ . Both of these measurements are sufficiently far from the Sun to be considered near free of ZL contamination.

As clearly shown in Fig. 9, our optical/NIR IGL measurements are inconsistent with the interpretation of the *HST*-based direct estimates as tentative measurements, but consistent as upper limits. As outlined in Bernstein (2007), the key issue is robust subtraction of bright foregrounds such as the DGL and the Zodiacal emission. The

discrepancy is less prominent between the direct measurements from deep-space probes such as the Pioneer 10/11 or the New Horizon mission but to a lesser extent. It would therefore seem that the likely issue, at least in comparison to the *HST* data, is with the subtraction of the ZL, which drops substantially as one moves outward in the Solar system, or potentially due to additional airglow contamination from the upper atmosphere. For completeness, we also include recent result from the dark cloud method (purple diamond; Mattila et al. 2017b), which excluded bright galaxies  $< \sim 22$  mag and resulted in  $11.6^{+4.4}_{-4.4}$   $\text{nW m}^{-2} \text{sr}^{-1}$  at 400 nm as an upper limit.

Hence some small tension does still remain between the deep space probe data, the dark cloud data, and the IGL data that as argued by Lauer et al. (2021) may leave some room for a diffuse COB component of unknown origin. One argument against this, is the strong agreement between the IGL data that are sensitive to the discrete COB, and the VHE data (discussed earlier) that are sensitive to both the discrete and diffuse COB. Hence we are in the intriguing situation where the IGL and VHE are fully consistent, but at low-level tension with the deep space platform and dark cloud data. An obvious solution is that the additional radiation being detected by the space-platform data may be associated with either the outer Solar system, additional DGL, or the outer Milky Way dark-matter Halo, i.e. local. Resolving this discrepancy will likely require improvements in all three methods.



Finally, in Fig. 9 we also show three recent models along with our data points. SHARK (Lagos et al. 2019; dashed green line) is a semi-analytical model of galaxy formation and evolution (SAM) extending from FUV to FIR, the model of Khaire & Srianand (2019, solid orange line) is a synthesis model of the EBL from FIR to high energy  $\gamma$ -rays, and Andrews et al. (2018, solid purple line) present a phenomenological model of the cosmic spectral energy distribution (CSED) based on simple forward modelling from an input CSFH. While all the models show good consistency they mostly lie outside of the error ranges of our data heralding the prospect of using our data to now test the models more stringently as our errors continue to improve.

In this work, we have shown that the optical/NIR IGL uncertainty has been improved (see Fig. 7) in the optical regime from 20 per cent (Driver et al. 2016b) to below 10 per cent. Fig. 6 highlights the dominant error across the magnitude range in the  $r$  band. This shows that in order to further improve IGL measurements, we need wider area data at brighter magnitudes as well as improved calibration, including filter conversions, at fainter magnitudes. Both of these will be satisfied through the WAVES and *HST* SKYSURF projects. The former will reprocess the entire VISTA VIKING/VST KiDS region increasing the wide area coverage from 230 deg<sup>2</sup> to 1300 deg<sup>2</sup>, while the SKYSURF project will include a complete reanalysis of *HST* data using PROFOUND with the opportunity to perform more robust colour corrections on a galaxy-by-galaxy basis. Both of these improvements have the potential to reduce the IGL uncertainty to <3 per cent.

In due course, the Rubin Observatory, *EUCLID*, the *Roman Space Telescope*, and *JWST* will potentially provide wider and deeper data to reach a potential accuracy of <1 per cent within 10–20 yr. In addition, the suitability of recent surveys such as Pan-STARRS, DES, the DESI Legacy Survey, and HyperSuprimeCam at Subaru should provide a promising pathway forward as our measurements improve.

## 6 MODELLING THE EBL

As outlined in the introduction, the COB (and CIB) is the radiation by-product of cosmic star formation over all time, and as such is directly predictable given a CSFH, and what we know about stellar evolution and dust attenuation. Recently, Driver et al. (2012) and Andrews et al. (2018) built models to predict the EBL (Driver et al. 2016b), and its subdivision by redshift into CSED slices. These models require as input a CSFH parametrization, stellar libraries, e.g. PEGASE2 or BC03 (Bruzual & Charlot 2003), an initial mass function (IMF), and simple axioms around metallicity evolution (typically linked to star formation), dust attenuation and dust emission, and, in the Andrews et al. (2018) case, the ability to incorporate obscured and unobscured AGN components. Here, we essentially repeat this process, but we now adopt the comprehensive package PROSPECT (Robotham et al. 2020). This package has been developed to both model and generate individual galaxy SEDs, with significant robustness, flexibility, and functionality. It also includes a sub-module to provide an EBL prediction from UV to FIR, given the kind of assumptions described above. PROSPECT therefore provides us with the opportunity to use the COB to constrain model inputs to the EBL code, and in particular the CSFH normalization (see B20; Robotham et al. 2020).

The CSFH is a fundamental empirical measurement describing the evolution of the galaxy population from the past to the present time. Empirically, the CSFH has been measured via a number of complementary methods i.e. broad-band and spectral line measurements (the compilation of measurements by Madau & Dickinson 2014, hereafter MD14). The core sampling technique results from

MAGPHYS (Driver et al. 2018, D18); VHE constraints (FL18); SED forensic reconstruction (Bellstedt et al. 2020b, B20) and IFU forensic reconstruction (Sánchez et al. 2019, S19; López Fernández et al. 2018, L18). On the whole the distinct methods for reconstructing the CSFH agree on the overall trend and shape, i.e. a rapid rise to cosmic noon at  $z \leq 2$ , and thereafter a gentle continuous decline. In detail, the range of CSFH measurements exhibit an uncertainty of almost a factor of 3 at cosmic noon (see Fig. 10). In this work, we attempt to reduce the uncertainty by including our COB measurements to the modelling as a new constraint.

### 6.1 A simple analytical representation of the cosmic star formation history

To predict the COB using the PROSPECT EBL model, we represent each measured CSFH as a simple analytical function for computational purposes. We elect to use the skewed normal function (SNORM), defined in PROSPECT as `massfunc_snorm` function given by equation (3), which can be defined by four free parameters:

$$\text{SFR}(\text{age}) = \text{mSFR} \times e^{-\frac{X(\text{age})^2}{2}}, \quad (3)$$

where  $X$  is age dependent and defined as

$$X(\text{age}) = \left( \frac{\text{age} - \text{mPeak}}{\text{mPeriod}} \right) \left( e^{\text{mSkew}} \right)^{\text{asinh}\left(\frac{\text{age} - \text{mPeak}}{\text{mPeriod}}\right)}, \quad (4)$$

where ‘age’ is in lookback time (Gyr) and the four free parameters are defined as

- (i) **mSFR**: Star formation rate normalization in units of  $\text{M}_\odot \text{yr}^{-1}$ ;
- (ii) **mPEAK**: The lookback age of the SFH peak in Gyr;
- (iii) **mPERIOD**: Time period of the star formation i.e. the standard deviation of the SFH period; and
- (iv) **mSKEW**: The skew of the SFH (0 for normal, < 0 for long tail to old ages and > 0 for long tail to young ages).

It is noted that mSFR is the peak SFR value and modifying its value scales the entire plot up and down without changing the shape and hence it also acts as a normalization parameter.

We fit each of our adopted CSFHs with the SNORM function and show the fitted values in Table 5 and also plotted as lines in Fig. 10. The solid gold line shows the raw CSFH values from B20 where the yellow shaded region shows the measurement uncertainty from the sampling of the MCMC chains that determine the SFH. In general, the SNORM parametrization is a reasonable fit to the various data and places all data sets on to a simple comparable footing, with perhaps the exception of the (S19) data set at very low redshift. Note, the (S19) study used a Salpeter IMF, and the values have been rescaled to a Chabrier IMF by multiplying by  $\times 0.63$  (MD14).

### 6.2 EBL predictions with PROSPECT

With a simple representation of the CSFH in place, we can now make our COB predictions using the PROSPECT EBL routine (see EBL vignette on github<sup>1</sup>). In brief, the PROSPECT prediction adopts the Chabrier IMF (Chabrier 2003) and defines the COB/CIB by condensing the full galaxy population down to a canonical representative galaxy intended to reflect a mean mass-weighted SED. This canonical representative SED, includes the following elements:

- (i) An invariant Chabrier IMF (Chabrier 2003).

<sup>1</sup><https://github.com/asgr/ProSpec>

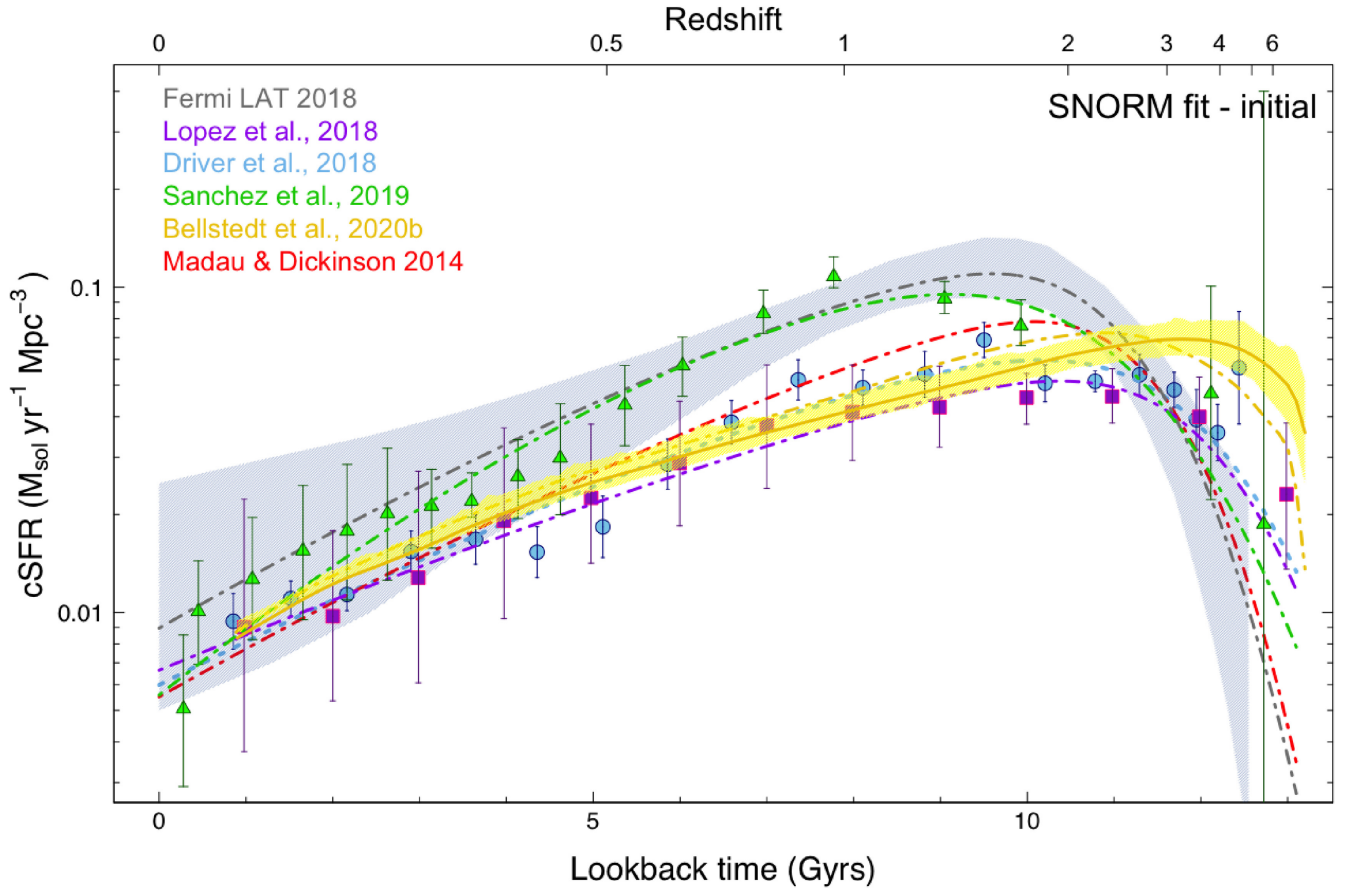


**Figure 10.** The cosmic star formation rate before our constraint using mSFR (the peak value) parameter (as described in text) shown for the various methods: SED core sampling in sky-blue (D18); VHE constraints in grey (FL18); SED forensic reconstruction in gold (B20); IFU forensic reconstruction in purple and green (López Fernández et al. 2018 and S19, respectively). We also show the curve from MD14 as the dashed red line. The solid gold line shows the raw CSFH value from B20.

**Table 5.** Free parameters obtained from the SNORM function and our best SFR and metallicity values for six different methods before and after rescaling.

Method	$m\text{SFR}_{\text{final}}$	$m\text{SFR}_{\text{initial}}$	$m\text{PEAK}$	$m\text{PERIOD}$	$m\text{SKEW}$	$Z_{\text{best}}$	$\chi^2_{\text{best}}$
Driver et al. (2018); D18	$0.069 \pm 0.001$	0.06	10.164	2.369	0.321	$0.017 \pm 0.003$	3.07
Madau & Dickinson (2014); MD14	$0.076 \pm 0.002$	0.078	10.077	1.884	0.354	$0.018 \pm 0.004$	2.94
Fermi-LAT Collaboration (2018); FL18	$0.074 \pm 0.001$	0.110	9.594	2.010	0.334	$0.025 \pm 0.006$	2.68
Sánchez et al. (2019); S19	$0.070 \pm 0.001$	0.095	9.114	2.393	0.229	$0.025 \pm 0.005$	3.37
Lopez Fernandez et al. (2018); L18	$0.066 \pm 0.001$	0.051	10.378	2.286	0.364	$0.019 \pm 0.004$	2.85
Bellstedt et al. (2020b); B20	$0.069 \pm 0.001$	0.073	10.94	2.074	0.394	$0.015 \pm 0.002$	3.55

(ii) Closed box stellar evolution using BC03 (Bruzual & Charlot 2003) simple stellar population libraries.

(iii) Two-components dust model to represent the birth clouds and the interstellar medium (ISM)

(iv) An FUV-IR attenuation prescription following the free form variant of the Charlot & Fall (2000) prescription (independent for each dust component).

(v) Energy-conserving flux redistribution to the far-IR using templates by Dale et al. (2014) (independent for each dust component).

(vi) Evolving gas-phase metallicity that tracks star formation, i.e. grows with the locked-up stellar mass (Driver et al. 2013).

In running our model for our canonical galaxy, we adopt the opacities ( $\tau_{\text{BC}} = 1$ ,  $\tau_{\text{ISM}} = 0.3$ ), temperatures/profile shapes ( $\alpha_{\text{BC}} = 1.75$ ,  $\alpha_{\text{ISM}} = 3.0$ ), and the default birth cloud/ISM power laws

( $-0.7$ , as recommended by Charlot & Fall 2000). These parameters represent the PROSPECT defaults, except for the  $\alpha_{\text{BC}}$  value that is increased from 1.0 to 1.75 implying slightly cooler dust, and was chosen to shift the predicted FIR dust peak to longer wavelengths to better align with the observed CIB measurements. With these parameters fixed throughout, we can now feed in the parametrized CSFH into the PROSPECT EBL routine to produce a full COB/CIB prediction of the EBL as observed at  $z = 0.0$ . The dashed lines in the left-hand panels of Fig. 11 show the resulting EBL predictions. Note that, for CSFH measurements that are normalized higher than the others (S19 and FL18), the resulting EBL overpredicts our EBL measurements. 125.0pt

For each of our six CSFH parametrizations, we now generate a grid of COB/CIB predictions, as viewed through the *ugriZYJHK<sub>s</sub>* filter-set, by fitting for a range of CSFH normalizations (mSFRs),

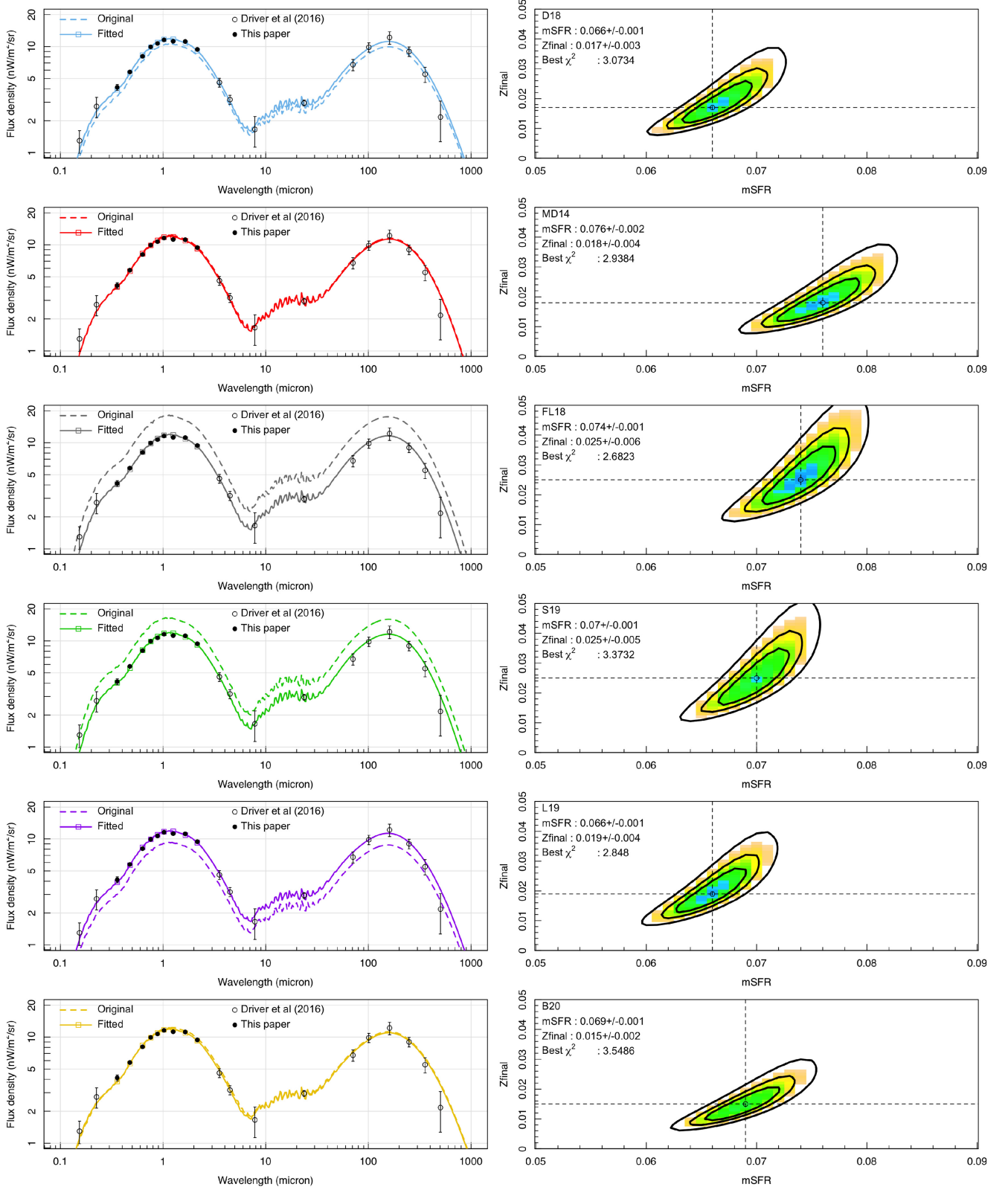


**Figure 11.** The reduced  $\chi^2$  analysis for each of our star formation histories showing the initial and final EBL model predictions compared to the data, and (right-hand panels) the 1, 2, and 3 $\sigma$  contours in the mSFR-Z<sub>final</sub> plane. The y-axis shows the final metallicities (Z<sub>final</sub>). This analysis has been summarized in Table 5.

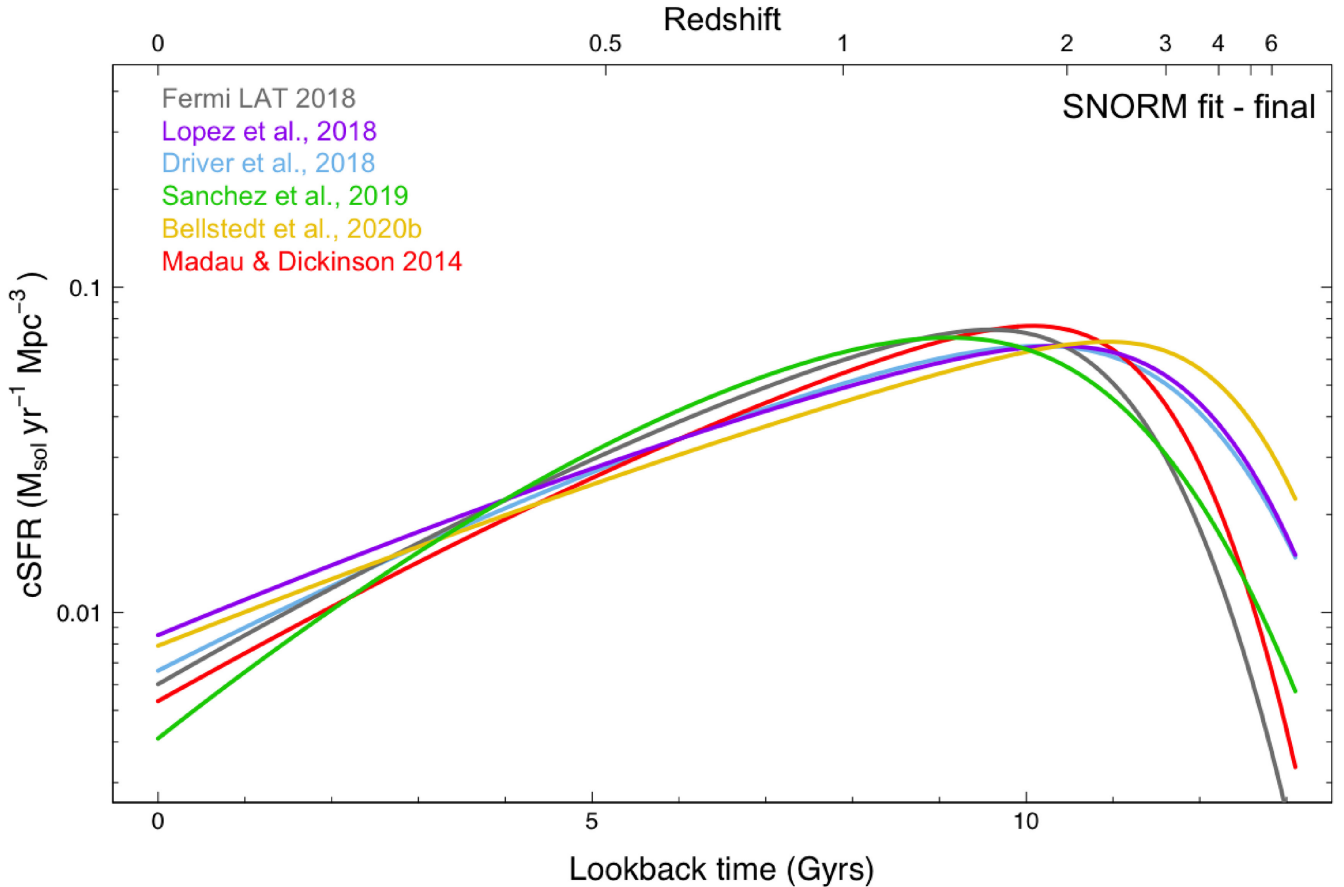


**Figure 12.** The cosmic star formation rate after our constraint.

and final metallicities ( $Z_{\text{final}}$ ). As discussed in detail by B20, the SED of a galaxy is influenced by not only the age distribution of the stellar population, but also the metallicity of the stellar population. It is therefore important for us to simultaneously fit for the modelled final gas-phase metallicity ( $Z_{\text{final}}$ ), in addition to the normalization of the CSFH (mSFR). Using the closed-box metallicity evolution prescription within PROSPECT, the shape of the metallicity evolution is prescribed by the build-up of stellar mass, but the target final metallicity value is a free parameter. Inherently, this value represents the light-weighted metallicity at which stars are forming at the present day, which could be interpreted as the light-weighted ISM metallicity. We note that this is not a measurement of the overall ‘cosmic’ gas-phase metallicity, as this approach is only sensitive to star-forming gas. Consequently, the  $Z_{\text{final}}$  parameter can be regarded as a kind of nuisance parameter, required for fitting in order to accurately model the metallicities of the stellar populations in the galaxy sample.

In order to compute the revised mSFR, we simply scale up and down the mSFR value until we get the best  $\chi^2$  between the EBL model prediction and the EBL data in the *ugriZYJHK<sub>s</sub>* bands. Each CIB/COB prediction is regressed against the COB data, the error-weighted (reduced)  $\chi^2$  values determined for each prediction, and the final best-fitting and error contours determined for each of our adopted CSFH representations. The model results, showing the original and final COB/CIB predictions, for each of our adopted CSFHs are shown in Fig. 11 (left-hand panels), along with the  $1\sigma$ ,  $2\sigma$ , and  $3\sigma$  confidence levels (right-hand panels).

Table 5 summarizes the result of the  $\chi^2$  analysis, showing the four initial free parameters of the SNORM function, the final metallicity, the

revised mSFR, and best  $\chi^2$ -value after applying the EBL constraint to each CSFH representation. Note that the reduced- $\chi^2$  values are reasonably distributed around unity, as would be expected if errors are reasonable and the model appropriately describes the data. The revised SNORM values represent a range of adjustments with the CSFHs of MD14 and B20 requiring the least rescaling and essentially fully consistent with their original specified values. The remaining CSFHs all required adjustment to match the COB/CIB data. Fig. 12 shows the set of CSFHs renormalized, and the scatter is notably reduced around cosmic noon from  $\times 3$  to  $< 30$  per cent.

Following renormalization against the COB/CIB, we can therefore report a peak value of  $0.067\text{--}0.075\text{ M}_{\odot}\text{ yr}^{-1}\text{ Mpc}^{-3}$  at  $z \sim 1.5\text{--}3$ . Hence this analysis provides an interesting additional constraint on CSFH measurements and provides strong support for the values reported by MD14 from core-sample style analysis, and the recent forensic measurement from  $\sim 7000$  GAMA galaxies by B20. The analysis is in the sense that the MD14 and B20 required the smallest adjustments of their initial mSFR values. It also provides some support for the adopted dust model parameters that well match the far-IR data (see Fig. 14). In future analysis, it should be possible to also fit for the dust parameters as our COB/CIB errors improve.

### 6.3 The stellar mass density

The top panel in Fig. 13 shows a zoom of the best-fitting EBL from *u* to *K<sub>s</sub>* band as obtained by PROSPECT using the renormalized D18 CSFH. We also show the associated prediction for the stellar mass density (SMD) based on this CSFH (bottom panel).



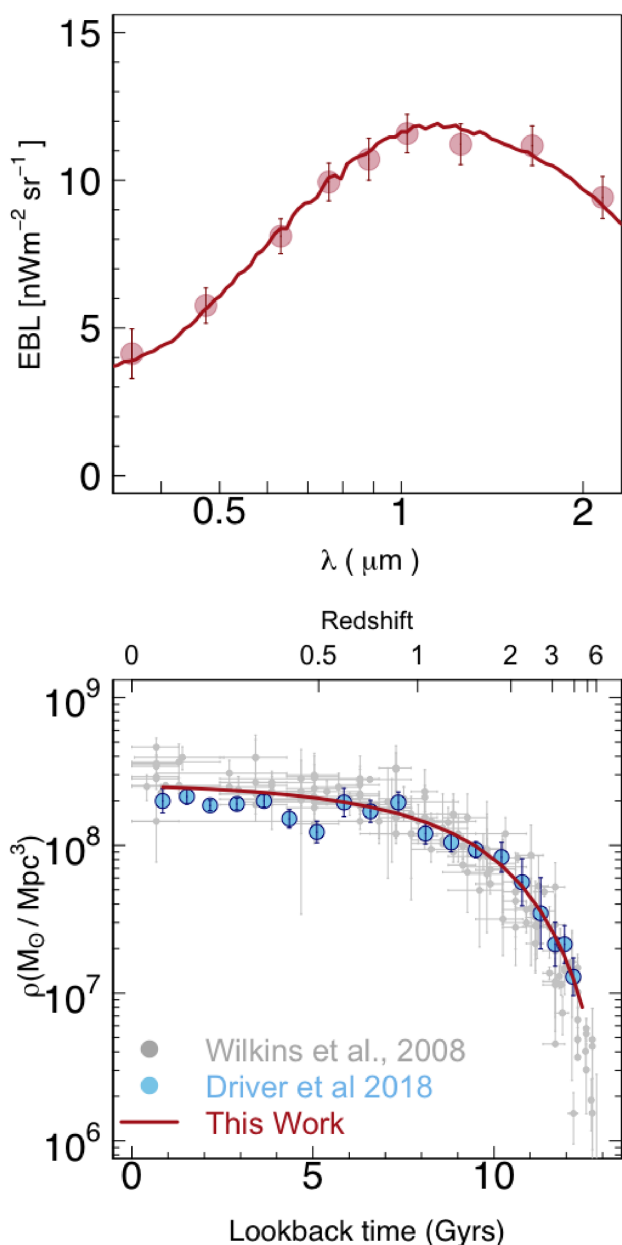


**Figure 13.** (top) The best-fitting EBL model from PROSPECT; (bottom) the derived SMD compared to data from Wilkins et al. (2008, grey), and Driver et al. (2018, blue).

This SMD prediction, shown as the red curve in the bottom panel of Fig. 13 compares well to data from Wilkins, Trentham & Hopkins (2008, grey data points) and D18 (blue data points), where the latter represents the full GAMA/G10-COSMOS/3D-*HST* combined data set, spanning almost the entire age of the Cosmos. In detail, we see that the model only just lies within the error bars of the data that are most likely a reflection of the fact that PROSPECT does produce slightly higher stellar masses, given the same data, than MAGPHYS (see Robotham et al. 2020, fig. 33, lower panel) which was used to determine the data points in D18. However, there are also two other plausible physical explanations. One is that mass-loss is very slightly higher than assumed for a Chabrier IMF. The second and perhaps more interesting is that such a discrepancy could potentially represent stripped or missing local mass, as the IGL is predominantly

derived from light production at intermediate redshifts while the SMD is measured locally (see Ashcraft et al. 2018 and Ashcraft 2018 PhD dissertation). Hence if some stellar mass is stripped from the progenitors of the present day population in the latter half of the Universe, this could manifest as a modest discrepancy between the EBL predicted SMD and that measured. The obvious way to distinguish, is by breaking the EBL into its constituent CSED time slices, where one might start to identify less energy than expected if mass is being stripped and not accounted for. The reverse is also true, in that a good match between the CSFH, SMD, and COB/CIB data suggests, mass stripping is a very small factor (few per cent), otherwise the predicted SMD would significantly overpredict the measured stellar-mass density. To bring our predicted SMD perfectly in line with the data, would require an offset of about 20 per cent, which is consistent with the 15 per cent stellar mass offset between MAGPHYS and PROSPECT (see Robotham et al. 2020; B20). The implication is that our results are consistent with mass stripping of anywhere from 0 to 10 per cent. This constraint is likely to be tightened as we improve both our stellar mass estimates of the nearby population, as well as our COB/CIB constraints.

#### 6.4 The final EBL and comparison to models

Finally, Fig. 14 presents our best-fitting EBL model based on the modified D18 CSFH, to the full COB and CIB data, shown as black data points. Note that the new IGL data from our revised number counts (*ugriZYJHK<sub>s</sub>*) are shown as closed black circles, and this is now complemented by our previous IGL results (Driver et al. 2016b) shown as open black circles to extend the plot to the UV, MIR, and FIR regimes. Overlaid are recent model predictions from our earlier phenomenological model (purple line; Andrews et al. 2018), data from the new SHARK semi-analytical model (green line; Lagos et al. 2019), and the recent Khaire & Srianand phenomenological model (orange line; Khaire & Srianand 2019). All provide reasonable descriptions of the observed distribution, with the optimized PROSPECT fit providing the closest match over not just the  $u - K_s$  regime but the entire FUV to FIR range. We provide our optimized model in electronic Table form, with Table 6 showing the first and last three lines of the data file, and advocate the use of these data as the best current representation of the COB and CIB. A related point to consider is that the comparison between SHARK and the observation at the FIR likely requires further analysis.

The cyan dashed line shows the EBL calculation from the EAGLE data.<sup>2</sup> We compute the predicted EBL from the EAGLE simulations (Schaye et al. 2015) by retrieving from the EAGLE public data base (McAlpine et al. 2016) all galaxies from  $z = 0$  to  $z = 9$  that had an observer-frame  $r$ -band flux  $> 0$  (i.e. a flux calculation was possible) and their full photometry in the bands GALEX FUV and NUV, SDSS  $u, g, r, i, z$ , UKIDSS  $Z, Y, J, H, K$ , WISE bands 1, 2, 3, and 4, MIPS 24 microns, IRAS 60 microns, PACS 70, 100, and 160 microns, SPIRE 250, 350, and 500 microns, and SCUBA2 450, and 850 microns. These fluxes were computed via post-processing of EAGLE galaxies using the radiative transfer code SKIRT (see Trayford et al. 2017 for details). For each redshift, we compute the implied projected sky area of a  $(100 \text{ cMpc})^2$  square assuming the EAGLE cosmology (Planck Collaboration XI 2014) and the energy contributed by that redshift,  $E(z)$ , as the sum of the fluxes of all galaxies at that redshift divided by the solid angle corresponding to the area above. We then integrate under the  $E(z)$  versus  $z$  curve to obtain the predicted EBL.

<sup>2</sup>Data obtained from the public data base (McAlpine et al. 2016).

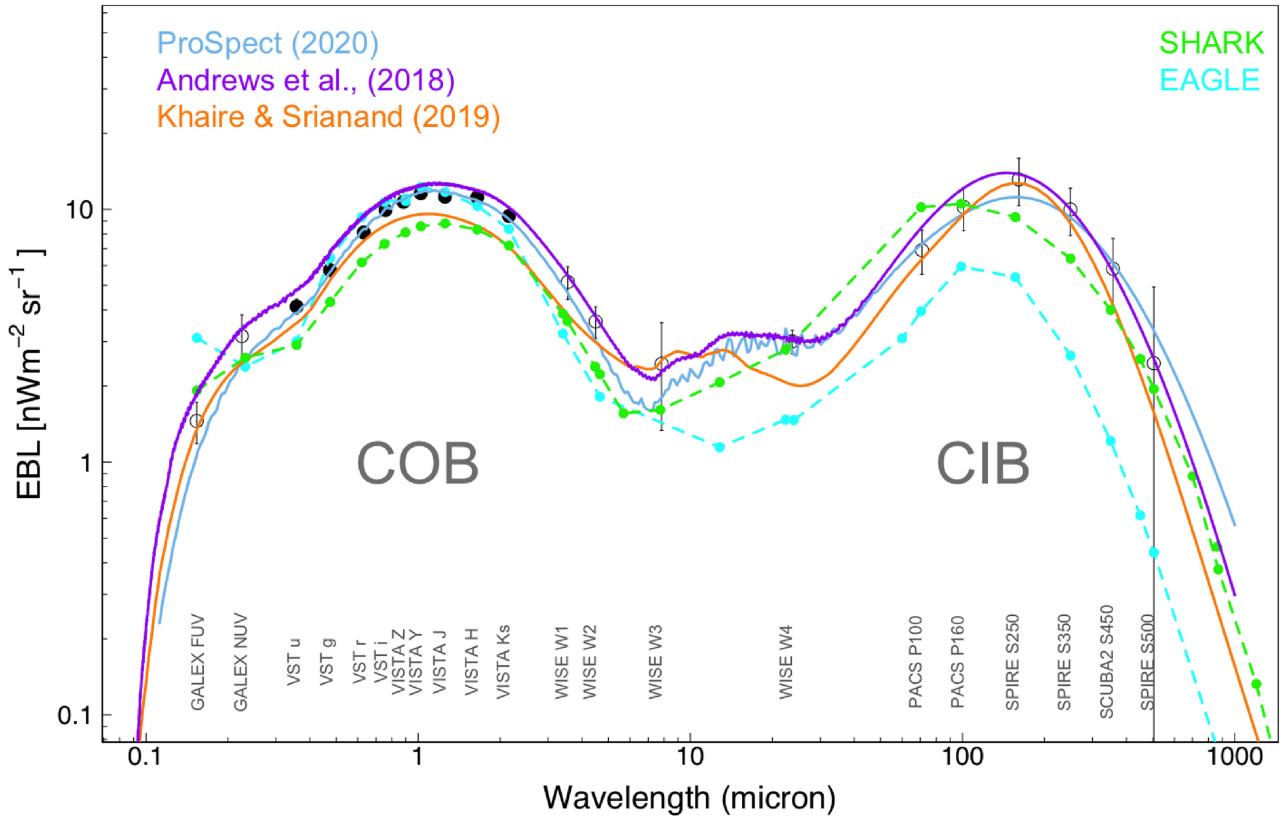


**Figure 14.** Final EBL model from Driver et al. (2018) in sky blue is compared to the other data from semi-analytical model (green), synthesis model (orange), and phenomenological model (purple). We overplotted the IGL data from  $u$  to  $K_s$  obtained from our number counts in closed circles combined with the IGL data for UV, mid-IR, and far-IR from Driver et al. (2016b) in open circles to present both CIB and COB. EAGLE data are shown in cyan.

**Table 6.** A sample of our EBL spectrum from PROSPECT. The full table in csv format (*filename : EBL\_model.csv*) is provided electronically as supplementary material. The first column identifies the wavelength in angstrom for a range of FUV to FIR and the second column shows the derived flux in the unit of ( $\text{nW m}^{-2} \text{sr}^{-1}$ ).

Wavelength ( $\text{\AA}$ )	Flux ( $\text{nW m}^{-2} \text{sr}^{-1}$ )
1122.0185	0.2305
1148.1536	0.2753
1174.8976	0.3160
...	...
9549925.9	0.6487
9772372.2	0.6046
10000000.0	0.5636

We note that the fluxes used to compute the predicted EBL for EAGLE, only include galaxies that have a number of (sub-)particles representing the galaxy's body of dust  $> 250$  (see Camps et al. 2018 for details). This roughly ignores about  $\approx 30$  per cent of galaxies with stellar masses  $> 10^{10} M_{\odot}$  at  $z < 0.4$ , which are expected to be bright in the optical and NIR given their large stellar mass. We hence consider the presented EBL here as a lower limit for EAGLE, but it's likely that the true EBL in the simulation is only 20–30 per cent higher in the optical-NIR, which is still  $\approx 50$  per cent lower than the observations indicate. The MIR–FIR part of the EBL, however, is

likely less affected by these limits, and hence the underprediction here is in tension with observations. Furthermore, there are reasons to believe the simulations are underestimates by 20–30 per cent. However, even if one incorporated this correction the simulations would still underpredict the EBL observations by 50 per cent. This is not necessarily surprising given the discrepancy in the predicted number counts of EAGLE and observations in the FIR bands (e.g. Cowley et al. 2019; Wang et al. 2019).

## 7 CONCLUSIONS

This paper presents a measurement of the optical part of the extragalactic background light via integrated galaxy number-counts to significantly greater accuracy than previous measurements, enabling us to use the COB data to place constraints on to the CSFH. The main results of this work are summarized as:

(i) We combined three complementary data sets and derived in relatively wide and deep fields the galaxy counts in the optical and NIR bands ( $ugriZYJHK_s$ ) from the GAMA, DEVILS, and various deep ground-based and *HST* data sets. The compilation of wide and deep data sets allows us to measure the galaxy number counts in a wide magnitude interval (spanning more than 15 magnitudes) across the multiwavelength filters. Where possible filter conversions have been applied to map our measurements on to the ESO VST/VISTA  $ugriZYJHK_s$  system. In general, our revised number-counts agree well with other published data in all bands and with significantly improved errors over the critical intermediate magnitude range that dominates the IGL signal.

(ii) From the number-count data, we determine the contribution in each magnitude interval to the total luminosity density. We fit a smooth spline and extrapolate over the entire magnitude range to derive the integrated flux density, or IGL, of discrete sources from a steradian of sky over the full path-length of the Universe and in each filter. Compared to previous results, we find a 5–15 per cent increase in our IGL measurements from  $u - K_s$ . We attribute this increase to several factors that include: PROFOUND’s propensity to recover closer to total fluxes, appropriate filter transformations, and improved accounting for the area lost to bright stars and their associated haloes (ghosting).

(iii) We compared our optical/NIR IGL measurements to VHE COB (i.e. those from Fermi-LAT, MAGIC, H.E.S.S., and VERITAS), and direct estimates from space platforms (*HST*, Pioneer 10/11, New Horizons). Our derived optical/NIR IGL results agree well within the errors with all VHE COB measurements, and those from the deep space based missions (i.e. Pioneer 10/11 and New Horizons). The implication is that significant uncertainty must exist in either or both our understanding of dust in the inner Solar system (ZL), or upper atmosphere Earth-shine in the *HST* data set.

(iv) The new optical/NIR IGL measurements include an improved error-analysis to manage the uncertainty introduced by CV. We assessed both systematic (zero-point, filter uncertainty, and CV), and random (spline fitting and Poisson) errors. In doing so we have reduced the uncertainty from  $\sim 20$  per cent to below  $\sim 10$  per cent. It can also be inferred that this analysis is now mostly dominated by systematic errors, and in particular CV at bright and intermediate magnitudes, and positioning issues (i.e. zero-point and filter conversions) at faint magnitudes. With the advent of the Rubin Observatory, *Euclid*, the *Roman Space Telescope*, and *JWST* there is a strong prospect to address these issues and reduce the errors closer to the 1 per cent mark.

(v) To model the EBL, we introduced the SNORM function fitted to the data of Driver et al. (2018). This is a simple four-parameters function that describes the adopted CSFHs extremely well. Using PROSPECT, we provide a prediction of the EBL and regress against our data to determine the optimal normalization of the SNORM function and the gas-phase metallicity evolution. The model provides an excellent fit from UV to far-IR and places strict constraints on the normalization of the CSFH with a constraint of  $0.066\text{--}0.076 M_{\odot} \text{ yr}^{-1} \text{ Mpc}^{-3}$  at cosmic noon. The constraint is in close agreement with that provided by Madau & Dickinson. We conclude that both the revised SNORM function and the MD14 result provide an excellent description of the CSFH that is fully consistent with both the stellar mass growth and energy production over all time.

## ACKNOWLEDGEMENTS

GAMA is a joint European-Australasian project based around a spectroscopic campaign using the Anglo-Australian Telescope. The GAMA input catalogue is based on data taken from the Sloan Digital Sky Survey and the UKIRT Infrared Deep Sky Survey. Complementary imaging of the GAMA regions is being obtained by a number of independent survey programmes including GALEX MIS, VST KiDS, VISTA VIKING, WISE, Herschel-ATLAS, GMRT, and ASKAP providing UV to radio coverage. GAMA is funded by the STFC (UK), the ARC (Australia), the AAO, and the participating institutions. The GAMA website is <http://www.gama-survey.org/>. Based on observations made with ESO Telescopes at the La Silla Paranal Observatory under program ID 179.A-2004.

DEVILS is an Australian project based around a spectroscopic campaign using the Anglo-Australian Telescope. The DEVILS input catalogue is generated from data taken as part of the ESO VISTA-

VIDEO (Jarvis et al. 2013) and UltraVISTA (McCracken et al. 2012) surveys. DEVILS is partly funded via Discovery Programs by the Australian Research Council and the participating institutions. The DEVILS website is <https://devilsurvey.org>. The DEVILS data are hosted and provided by AAO Data Central.<sup>3</sup> Parts of this research were conducted by the Australian Research Council Centre of Excellence for All Sky Astrophysics in 3 Dimensions (ASTRO 3D) through project number CE170100013.

This research is supported by the University Postgraduate Awards (UPA) by the University of Western Australia Scholarships Committee and the awarded by the Astronomical Society of Australia.

This work was supported by resources provided by the Pawsey Supercomputing Centre with funding from the Australian Government and the Government of Western Australia.

MS has been supported by the European Union’s Horizon 2020 Research and Innovation programme under the Maria Skłodowska-Curie grant agreement (no. 754510), the Polish National Science Centre (UMO-2016/23/N/ST9/02963), and the Spanish Ministry of Science and Innovation through the Juan de la Cierva-formacion programme (FJC2018-038792-I).

## DATA AVAILABILITY

The data underlying this article are derived from three distinct sources as described below:

- (1) The GAMA catalogue (GAMAKiDSVIKINGv01.fits) is publicly available via a collaboration request (<http://www.gama-survey.org>).
- (2) The DEVILS (<http://www.devilsurvey.org>) catalogue (DEV-ILSProFoundPhotomv01) is currently available for internal team use and will be presented in Davies et al., in preparation, and subsequently publicly releases through data central (<https://datacentral.org.au/>).
- (3) The *HST* data are obtained from Driver et al. (2016b).

All the data products that are used and/or derived in this work are available on request.

## REFERENCES

- Abeysekara A. U. et al., 2019, *ApJ*, 885, 150  
 Aharonian F. et al., 2006, *Nature*, 440, 1018  
 Ahnen M. L. et al., 2016, *A&A*, 590, A24  
 Aihara H. et al., 2018, *PASJ*, 70, S4  
 Andrews S. K., Driver S. P., Davies L. J. M., Lagos C. d. P., Robotham A. S. G., 2018, *MNRAS*, 474, 898  
 Ashcraft T. A. et al., 2018, *PASP*, 130, 064102  
 Bellstedt S. et al., 2020a, *MNRAS*, 496, 3235  
 Bellstedt S. et al., 2020b, *MNRAS*, 498, 5581 (B20)  
 Bernstein R. A., 1999, in Bunker A. J., van Breugel W. J. M., eds, *The High-Redshift Universe: Galaxy Formation and Evolution at High Redshift*, Proceedings of a conference held in Berkeley, CA, 21-24 June, 1999. ASP Conference Proceedings, Vol. 193, p. 487  
 Bernstein R. A., 2007, *ApJ*, 666, 663  
 Bernstein R. A., Freedman W. L., Madore B. F., 2002, *ApJ*, 571, 85  
 Biteau J., 2013, in Cambresy L., Martins F., Nuss E., Palacios A., eds, *SF2A-2013: Proc. Annual meeting of the French Society of Astronomy and Astrophysics*, p. 303  
 Biteau J., Williams D. A., 2015, *ApJ*, 812, 60  
 Bravo M., Lagos C. d. P., Robotham A. S. G., Bellstedt S., Obreschkow D., 2020, *MNRAS*, 497, 3026  
 Bruzual G., Charlot S., 2003, *MNRAS*, 344, 1000

<sup>3</sup><https://datacentral.org.au/>



- Camps P. et al., 2018, *ApJS*, 234, 20
- Capak P. et al., 2007, *ApJS*, 172, 99
- Chabrier G., 2003, *PASP*, 115, 763
- Charlot S., Fall S. M., 2000, *ApJ*, 539, 718
- Cooray A. et al., 2009, In *astro2010: The Astronomy and Astrophysics Decadal Survey*. Science White Papers, no. 54
- Cooray A. et al., 2012, in Tuffs R. J., Popescu C. C., eds, *Proc. IAU Symp.* 284, *The Spectral Energy Distribution of Galaxies*, p. 482
- Cowley W. I., Lacey C. G., Baugh C. M., Cole S., Frenk C. S., Lagos C. d. P., 2019, *MNRAS*, 487, 3082
- Dale D. A., Helou G., Magdis G. E., Armus L., Díaz-Santos T., Shi Y., 2014, *ApJ*, 784, 83
- Davies L. J. M. et al., 2018, *MNRAS*, 480, 768
- De Pontieu B. et al., 2014, *Sol. Phys.*, 289, 2733
- Desai A. et al., 2017, *ApJ*, 850, 73
- Dole H. et al., 2006, *A&A*, 451, 417
- Domínguez A. et al., 2011, *MNRAS*, 410, 2556
- Driver S., 2020, in *The Build-Up of Galaxies through Multiple Tracers and Facilities, 2nd Australia-ESO Joint Conference, held 17-21 February, 2020 in Perth, Western Australia*, Online at <https://www.icrar.org/conferences/aus-eso-ii/>, esoaus2020. p. 7
- Driver S. P., GAMA Team, 2016, in Skillen I., Balcells M., Trager S., eds, *ASP Conference Series*, Vol. 507, *Multi-Object Spectroscopy in the Next Decade: Big Questions, Large Surveys, and Wide Fields*. Proceedings of a conference held at Teatro Circo de Marte, Santa Cruz de La Palma, Canary Islands, Spain on 2-6 March 2015. Astronomical Society of the Pacific, San Francisco, p. 269
- Driver S. P., Robotham A. S. G., 2010, *MNRAS*, 407, 2131
- Driver S. P. et al., 2011, *MNRAS*, 413, 971
- Driver S. P. et al., 2012, *MNRAS*, 427, 3244
- Driver S. P., Robotham A. S. G., Bland-Hawthorn J., Brown M., Hopkins A., Liske J., Philipps S., Wilkins S., 2013, *MNRAS*, 430, 2622
- Driver S. P. et al., 2016a, *MNRAS*, 455, 3911
- Driver S. P. et al., 2016b, *ApJ*, 827, 108
- Driver S. P. et al., 2018, *MNRAS*, 475, 2891 (D18)
- Edge A., Sutherland W., Kuijken K., Driver S., McMahon R., Eales S., Emerson J. P., 2013, *The Messenger*, 154, 32
- Fermi-LAT Collaboration, 2018, *Science*, 362, 1031 (FL18)
- Fontana A. et al., 2014, *A&A*, 570, A11
- Frayser D. T. et al., 2009, *AJ*, 138, 1261
- Gaia Collaboration, 2016, *A&A*, 595, A2
- Giavalisco M. et al., 2004, *ApJ*, 600, L93
- González-Fernández C. et al., 2018, *MNRAS*, 474, 5459
- Grazian A. et al., 2009, *A&A*, 505, 1041
- Grogin N. A. et al., 2011, *ApJS*, 197, 35
- Hauser M. G., Dwek E., 2001, *ARA&A*, 39, 249
- HESS Collaboration, 2018, *MNRAS*, 476, 4187
- Hill R., Masui K. W., Scott D., 2018, *Appl. Spectrosc.*, 72, 663
- Hopkins A. M. et al., 2013, *MNRAS*, 430, 2047
- Inoue Y., Inoue S., Kobayashi M. A. R., Makiya R., Niino Y., Totani T., 2013, *ApJ*, 768, 197
- Jarvis M. J. et al., 2013, *MNRAS*, 428, 1281
- Kaiser N. et al., 2002, in Tyson J. A., Wolff S., eds, *Proc. SPIE Conf. Ser.* Vol. 4836, *Survey and Other Telescope Technologies and Discoveries*. SPIE, Bellingham, p. 154
- Kashlinsky A., 2006, *New Astron. Rev.*, 50, 208
- Kawara K., Matsuoka Y., Sano K., Brandt T. D., Sameshima H., Tsumura K., Oyabu S., Ienaka N., 2017, *PASJ*, 69, 31
- Keenan R. C., Barger A. J., Cowie L. L., Wang W. H., 2010, *ApJ*, 723, 40
- Khaire V., Srianand R., 2019, *MNRAS*, 484, 4174
- Kim M. G., Matsumoto T., Lee H. M., Jeong W.-S., Tsumura K., Seo H., Tanaka M., 2019, *PASJ*, 71, 82
- Kuijken K. et al., 2019, *A&A*, 625, A2
- Lagache G., Abergel A., Boulanger F., Désert F. X., Puget J. L., 1999, *A&A*, 344, 322
- Lagos C. d. P. et al., 2019, *MNRAS*, 489, 4196
- Lauer T. R. et al., 2021, *ApJ*, 906, 77
- Leinert C., Richter I., Pitz E., Planck B., 1981, *A&A*, 103, 177
- Liske J. et al., 2015, *MNRAS*, 452, 2087
- López Fernández R. et al., 2018, *A&A*, 615, A27
- McAlpine S. et al., 2016, *Astron. Comput.*, 15, 72
- McCracken H. J. et al., 2012, *A&A*, 544, A156
- Madau P., Dickinson M., 2014, *ARA&A*, 52, 415 (MD14)
- Madau P., Pozzetti L., 2000, *MNRAS*, 312, L9
- MAGIC Collaboration, 2008, *Science*, 320, 1752
- Matsumoto T. et al., 2005, *ApJ*, 626, 31
- Matsuoka Y., Ienaka N., Kawara K., Oyabu S., 2011, *ApJ*, 736, 119
- Mattila K., Väisänen P., 2019, *Contemp. Phys.*, 60, 23
- Mattila K., Lehtinen K., Väisänen P., von Appen-Schnur G., Leinert C., 2012, in Tuffs R. J., Popescu C. C., eds, *Proc. IAU Symp.* 284, *The Spectral Energy Distribution of Galaxies*, p. 429
- Mattila K., Lehtinen K., Väisänen P., von Appen-Schnur G., Leinert C., 2017a, *MNRAS*, 470, 2133
- Mattila K., Väisänen P., Lehtinen K., von Appen-Schnur G., Leinert C., 2017b, *MNRAS*, 470, 2152
- Moffett A. J. et al., 2016, *MNRAS*, 462, 4336
- Penzias A. A., Wilson R. W., 1965, *ApJ*, 142, 419
- Pierre M. et al., 2004, *J. Cosmol. Astropart. Phys.*, 2004, 011
- Pilbratt G. L. et al., 2010, *A&A*, 518, L1
- Planck Collaboration XI, 2014, *A&A*, 571, A11
- Puget J. L., Abergel A., Bernard J. P., Boulanger F., Burton W. B., Desert F. X., Hartmann D., 1996, *A&A*, 308, L5
- Rafelski M. et al., 2015, *AJ*, 150, 31
- Robotham A. S. G., Davies L. J. M., Driver S. P., Koushan S., Taranu D. S., Casura S., Liske J., 2018, *MNRAS*, 476, 3137
- Robotham A. S. G., Bellstedt S., Lagos C. d. P., Thorne J. E., Davies L. J., Driver S. P., Bravo M., 2020, *MNRAS*, 495, 905
- Sánchez S. F. et al., 2019, *MNRAS*, 482, 1557 (S19)
- Sanders D. B. et al., 2007, *ApJS*, 172, 86
- Schaye J. et al., 2015, *MNRAS*, 446, 521
- Scott D., 2000, in Courteau S., Willick J., eds, *ASP Conf. Ser.* Vol. 201, *Cosmic Glows: A CMB Review*, p. 403
- Scoville N. et al., 2007, *ApJS*, 172, 1
- Taniguchi Y. et al., 2007, *ApJS*, 172, 9
- Teplitz H. I. et al., 2013, *AJ*, 146, 159
- Totani T., Yoshii Y., Iwamuro F., Maihara T., Motohara K., 2001, *ApJ*, 550, L137
- Trayford J. W. et al., 2017, *MNRAS*, 470, 771
- VERITAS Collaboration, 2011, *Science*, 334, 69
- Vernet J., D'Odorico S., Christensen L., Dekker H., Mason E., Modigliani A., Moehler S., 2009, *The Messenger*, 138, 4
- Virani S. N., Treister E., Urry C. M., Gawiser E., 2006, *AJ*, 131, 2373
- Wang L., Pearson W. J., Cowley W., Trayford J. W., Béthermin M., Gruppioni C., Hurley P., Michałowski M. J., 2019, *A&A*, 624, A98
- Wilkins S. M., Trentham N., Hopkins A. M., 2008, *MNRAS*, 385, 687
- Windhorst R. A. et al., 2011, *ApJS*, 193, 27
- Windhorst R. A. et al., 2018, *ApJS*, 234, 41
- Wright E. L., 2004, *New Astron. Rev.*, 48, 465
- Wright E. L. et al., 2010, *AJ*, 140, 1868
- Xu C. K. et al., 2005, *ApJ*, 619, L11
- Zemcov M. et al., 2013, *ApJS*, 207, 31
- Zemcov M., Immel P., Nguyen C., Cooray A., Lisse C. M., Poppe A. R., 2017, *Nat. Commun.*, 8, 15003

## SUPPORTING INFORMATION

Supplementary data are available at [MNRAS](#) online.

### EBL\_model.csv

Please note: Oxford University Press is not responsible for the content or functionality of any supporting materials supplied by the authors. Any queries (other than missing material) should be directed to the corresponding author for the article.

This paper has been typeset from a  $\text{\LaTeX}$  file prepared by the author.